

ESTIMATION OF EXPECTED EULER CHARACTERISTIC CURVES OF NONSTATIONARY SMOOTH GAUSSIAN RANDOM FIELDS

BY ARMIN SCHWARTZMAN^{*†}, FABIAN TELSCHOW^{*}, DAN CHENG[‡] AND PRATYUSH PRANAV[§]

Division of Biostatistics, University of California, San Diego^{},
Halicioğlu Data Science Institute, University of California, San Diego[†],
School of Mathematical and Statistical Sciences, Arizona State University[‡]
and Département de Physique, Ecole Normale Supérieure de Lyon[§]*

The expected Euler characteristic (EEC) curve of excursion sets of a Gaussian random field is used to approximate the distribution of its supremum for high thresholds. Viewed as a function of the excursion threshold, the EEC is expressed by the Gaussian kinematic formula (GKF) as a linear function of the Lipschitz-Killing curvatures (LKC) of the field, which solely depend on the domain and covariance function of the field. So far its use for non-stationary Gaussian fields over non-trivial domains has been limited because in this case the LKCs are difficult to estimate. In this paper, consistent estimators of the LKCs are proposed as linear projections of “pinned” observed Euler characteristic curves and a linear parametric estimator of the EEC curve is obtained, which is more efficient than its nonparametric counterpart for repeated observations. A multiplier bootstrap modification reduces the variance of the estimator, and allows estimation of LKCs and EEC of the limiting field of non-Gaussian fields satisfying a functional CLT. The proposed methods are evaluated using simulations of 2D fields and illustrated in thresholding of 3D fMRI brain activation maps and cosmological simulations on the 2-sphere.

1. Introduction. Suppose f is a mean zero, variance one, smooth Gaussian random field with unknown covariance function over a compact set $S \subset \mathbb{R}^D$ with piecewise \mathcal{C}^2 -boundary satisfying the assumptions for the Gaussian Kinematic formula (GKF), c.f. [2, Theorem 12.4.2].

For any excursion threshold u , let $A(u) = \{s \in S : f(s) \geq u\}$ denote the excursion set of the field f above the level u and let $\chi(u)$ denote the empirical Euler characteristic (EC) of the set $A(u)$. Recall that the EC of a set in 1D counts the number of connected components, in 2D counts the number of connected components minus the number of holes and in 3D counts the number of connected components minus the number of holes plus the number of hollows. Seen as a function, $u \mapsto \chi(u)$ is called the *EC curve* of the field f .

The Gaussian kinematic formula [2] states that the expected Euler characteristic (EEC) of the set $A(u)$ can be expressed as a linear combination

$$(1) \quad \text{EEC}(u) = \mathbb{E}[\chi(u)] = \mathcal{L}_0 \Phi^+(u) + \sum_{d=1}^D \mathcal{L}_d \rho_d(u)$$

of the so-called EC-densities

$$(2) \quad \rho_d(u) = (2\pi)^{-(d+1)/2} H_{d-1}(u) e^{-u^2/2}, \quad d = 1, \dots, D,$$

where H_d is the d -th Hermite polynomial and $\Phi^+(u) = \mathbb{P}(N(0, 1) > u)$. The linear coefficients $\mathcal{L}_0, \dots, \mathcal{L}_D$ are called the Lipschitz-Killing curvatures (LKC) of S and are intrinsic volumes of S considered as a Riemannian manifold endowed with a Riemannian metric induced by f , c.f. [2, Chapter 12].

The LKCs contain all the necessary information about the domain and the covariance function of the field to compute the EEC. The LKC of order 0 is simply the EC of the domain S and does not depend on the covariance function, so it is known for a given domain. The other LKCs, however, do depend on the unknown covariance function and need to be estimated.

The GKF is remarkable for its simplicity. It allows to express the EEC curve as a linear combination of $D + 1$ known functions with coefficients given by the LKCs and it shows that the EEC curve is a smooth function, even though the observed EC curves are not continuous in u but piecewise constant, with jumps at the heights of the critical points of the field.

Since the EEC curve is an excellent approximation of the tail distribution of the supremum of the field [35], the EEC curve has been extensively used to set the significance threshold for control of the family-wise error rate (FWER), particularly in neuroimaging studies [39, 42, 23]. Doing so, however, has been possible only by assuming that the covariance function has a particular simple form that enables computation of the LKCs analytically, e.g. isotropic with a Gaussian shape. This assumption has been recently called into question, claiming that it has led to too many false positive findings and lack of reproducibility [12]. It is therefore important to develop inference methods that do not rely on such strong assumptions about the noise field.

Notably, even knowing the functional form of the possibly non-stationary covariance function exactly is generally not very helpful. While the LKCs can be written as integrals of covariances of partial derivatives of the field [2, Thm 12.4.1, Thm 12.4.2], these integrals are hard to evaluate analytically, or even numerically, for arbitrary domains of dimension higher than 1, such

as the cortical surface of a brain. Even in the study of the cosmic microwave background (CMB) radiation, where an isotropic field over the sphere is an appropriate model, evaluation of the LKCs on the sphere is computationally difficult.

Estimation from data gives an alternate route. Given an i.i.d. sample of random fields on the same domain, we show in this paper that the LKCs can be consistently estimated as projections of the EC curves onto the EC densities (2). We call this the Hermite projection estimator (HPE) of the LKCs. This estimator leads to a linear and smooth parametric estimator of the EEC curve, which we also call HPE, for which confidence bands can be obtained via a functional central limit theorem (fCLT). This estimator is shown to be more efficient than its nonparametric counterpart, obtained by simply averaging the observed EC curves.

As an illustrative example, Figure 1(top row) shows an isotropic field and its corresponding empirical EC curve. Note the roughness of the empirical EC curve. The “smooth” EC curve is the projection of the empirical EC curve onto the EC densities, yielding an estimate of EEC from a single realization. The bottom row shows estimation from multiple realizations of the field. Note that a nonparametric estimate may be also obtained by pointwise averaging of the empirical EC curves, but the smooth estimate obtained from the smooth EC curves is closer to the true EEC. Simulations show that the smooth estimator has in fact lower variance.

As shown in Section 6.1 the HPE can be seen as a continuous version of the linear regression method proposed earlier in [1] and was inspired by that idea. The main advantage of the functional approach advocated here is that it leads to simple and elegant expressions for the estimator (c.f., Theorem 1) and its associated covariance, equation (11). In Sections 2.3, 2.4 and 2.5 we also provide proofs of unbiasedness, consistency and asymptotic normality of the proposed LKC and EEC estimators, none of which is done in the more empirical approach of [1]. Moreover, a byproduct of the proof of Theorem 2 is the conjectured theoretical property of $\text{Cov}[\chi(u), \chi(u')]$ that it decays faster than any polynomial in u, u' , c.f., Corollary 1.

Additionally, for applications in FWER inference, we show in Theorem 5 that our estimator of the expected EEC curve leads to a consistent estimator of the detection threshold and we derive confidence intervals for it based on a CLT.

In real data applications the assumption of Gaussianity for the HPE is too strict. Usually, either non-Gaussian observed data or, for example if the variance of the data is unknown, standardized residuals, need to be used as input into the HPE. The latter are – even if the data is Gaussian – usually

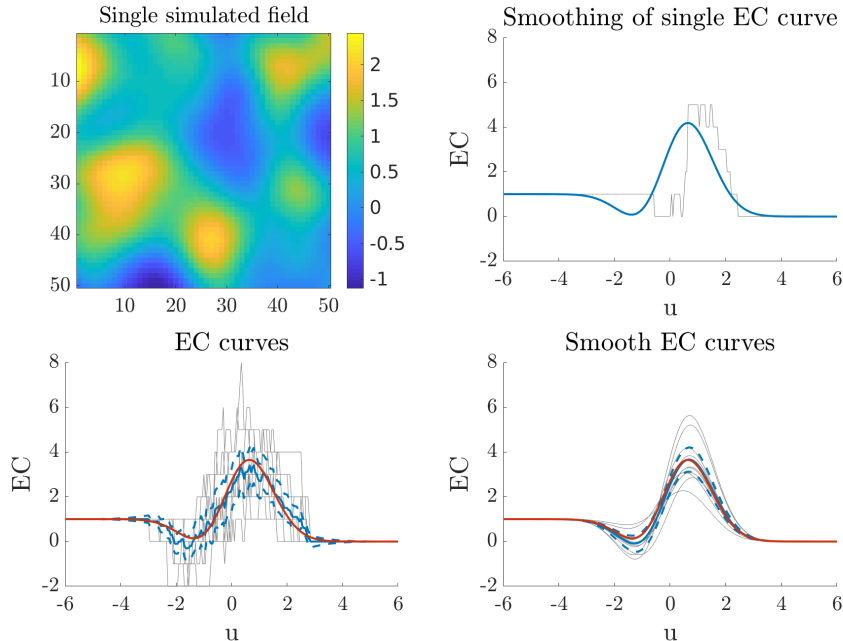


FIG 1. (Top left) A single realization of an isotropic Gaussian random field produced as convolution of white noise with a Gaussian kernel with standard deviation $\nu = 5$. (Top right) The corresponding empirical EC curve (gray) and smoothed EC curve (blue). (Bottom left) EC curves (gray) for $N = 10$ realizations of the field and their average (blue). (Bottom right) The corresponding smoothed EC curves (gray) and their pointwise average (blue), which is the estimated EEC curve. The dashed blue lines are pointwise 95% confidence bands for the true EEC curve. In both bottom panels, the true EEC curve is superimposed in red.

non-Gaussian fields, which leads to biased estimation of the LKCs using the HPE. Thus, using a Gaussian multiplier bootstrap, we generalize in Section 2.7 the HPEs to samples fulfilling a fCLT in order to estimate the EEC and LKCs of their limiting Gaussian field, which are often of interest for inference in applications, e.g., [42, 33]. We call this the bootstrap Hermite projection estimator (bHPE). Surprisingly, the bHPE actually has substantially less variance than the HPE as discovered in our simulations and therefore is preferable even for Gaussian input data. Possible reasons are discussed in Section 6.3.

In Section 4 we use simulations to demonstrate the theoretical properties and the finite sample performance of the proposed estimators for Gaussian, non-Gaussian and non-stationary fields on a 2D rectangular domain. Performances are compared to a method (IsotE) from [19] specifically tailored to

isotropic processes (currently the state of art in the neuroimaging package SPM12) and the warping-to-isotropy transformation (WarpE) of [41, 36], which applies to non-isotropic fields. In most cases we find that the bHPE gives comparable or even better results than its competitors. While WarpE performs well in our simulations and is a more direct, geometric approach and far less parametric estimator of LKCs than the bHPE, the latter offers a conceptually and computationally simpler approach that is equally effective with the additional advantage that derivatives and integrals of the fields do not need to be numerically approximated, see Theorem 1.

To further emphasize the flexibility of our proposed estimator, it is applied in Section 5 to real data applications with non-trivial domains. First, we study an fMRI data analysis example [22], where the domain of the field is the human brain and perform FWER inference on voxelwise activation in a “false belief task” experiment. Second, we illustrate the method using cosmological simulations [28] on a complex, non-trivial subset of the 2-sphere in order to compare the physical model with actual observed CMB data from Planck [27].

2. Estimation of the LKCs and the EEC for Gaussian fields.

2.1. *LKCs as functionals of the EC curve.* We begin with the following observation. Because of the orthogonality of the Hermite polynomials with respect to $e^{-u^2/2}$,

$$(3) \quad \int_{-\infty}^{\infty} H_{d-1}(u)H_{d'-1}(u)e^{-u^2/2} du = \sqrt{2\pi}(d-1)!\delta_{dd'}, \quad d, d' = 1, 2, \dots,$$

where $\delta_{dd'}$ is the Kronecker delta, it follows from (1) that for any $d = 1, \dots, D$, the LKC \mathcal{L}_d can be recovered from the EEC via

$$(4) \quad \mathcal{L}_d = \frac{(2\pi)^{d/2}}{(d-1)!} \int_{-\infty}^{\infty} H_{d-1}(u) \{ \text{EEC}(u) - \mathcal{L}_0 \Phi^+(u) \} du.$$

Let $\text{EEC}^\circ = \text{EEC} - \mathcal{L}_0 \Phi^+$ be the “pinned” EEC curve, pinned in the sense that it tends to 0 for both small and large u , since $\lim_{u \rightarrow \infty} \text{EEC}(u) = 0$ and $\lim_{u \rightarrow -\infty} \text{EEC}(u) = \mathcal{L}_0$. Then the operation (4) can be seen as a linear functional $\mathcal{L}_d = \mathcal{H}_d\{\text{EEC}^\circ\}$ by

$$(5) \quad \mathcal{H}_d(g) = \frac{(2\pi)^{d/2}}{(d-1)!} \int_{-\infty}^{\infty} H_{d-1}(u)g(u) du, \quad d = 1, 2, \dots$$

where $\mathcal{H}_d : F(\mathbb{R}) \rightarrow \mathbb{R}$ is defined over the set of functions in \mathbb{R} , where the integral is finite.

The functional (5) can also be seen as a linear projection operator. From (3) it follows that the EC densities (2) are orthogonal with respect to the inner product

$$(6) \quad \langle x, y \rangle = \int_{-\infty}^{\infty} x(u)y(u)e^{u^2/2} du,$$

defined for any two functions $x(u)$, $y(u)$ such that $|x|^2 = \langle x, x \rangle < \infty$ and $|y|^2 = \langle y, y \rangle < \infty$. In fact,

$$(7) \quad \langle \rho_d, \rho_{d'} \rangle = \int_{-\infty}^{\infty} \rho_d(u)\rho_{d'}(u)e^{u^2/2} du = (2\pi)^{-(d+1/2)}(d-1)!\delta_{dd'}.$$

In this sense, the linear functional (5) is equal to the projection coefficient

$$(8) \quad \mathcal{H}_d\{\cdot\} = \frac{\langle \cdot, \rho_d \rangle}{|\rho_d|^2}.$$

In particular, (1) indicates that $\mathcal{L}_d = \mathcal{H}_d\{\text{EEC}^\circ\}$ is the coefficient of ρ_d in the expansion of EEC° in the orthogonal basis $\{\rho_1, \dots, \rho_D\}$.

REMARK. The functional (5), which we may call *Hermite projector* for easier reference, is different in both quality and purpose from two other Hermite transforms previously defined in signal processing [21] and computer science [20], although all share the common feature of using the Hermite polynomials in their definitions.

2.2. *Estimation of the LKCs.* Because \mathcal{L}_0 is the EC of S , and so independent of the structure of f , it is known and need not be estimated. Given the empirical EC curve χ , formed by the EC of the excursion sets $A(u)$ of f above u for all thresholds $u \in \mathbb{R}$, we define the ‘‘pinned’’ EC curve

$$(9) \quad \chi^\circ = \chi - \mathcal{L}_0\Phi^+.$$

It is pinned again in the sense that it tends to 0 for both small and large u , since $\lim_{u \rightarrow \infty} \chi(u) = 0$ and $\lim_{u \rightarrow -\infty} \chi(u) = \mathcal{L}_0$ in probability. Applying the functional (5) yields the estimator

$$(10) \quad \hat{\mathcal{L}}_d = \mathcal{H}_d\{\chi^\circ\} = \frac{(2\pi)^{d/2}}{(d-1)!} \int_{-\infty}^{\infty} H_{d-1}(u)\chi^\circ(u) du,$$

which we may call the *Hermite projection estimator* (HPE) of the LKC \mathcal{L}_d , since it is based on the projection (8). Note that the integral is well

defined, since $\chi_0(u)$ is exponentially decaying outside the interval $[u_0, u_M]$ and bounded on it. Here u_0, u_M denote the values of the global minima and maxima, respectively, of the empirical f . Comparing with (4), the estimator $\hat{\mathcal{L}}_d$ plays the role of the “observed” LKC of order d of the field f .

As we shall see in Theorem 1 below, the integral in (10) can be avoided and the estimator can be computed simply as linear combination of polynomials in critical values of f .

2.3. Properties of the Hermite projection estimator. Heuristically, from equations (4) and (10) by interchanging integration and expectation we obtain that $\hat{\mathcal{L}}_d$ is unbiased. Moreover, let $\hat{\mathcal{L}} = (\hat{\mathcal{L}}_1, \dots, \hat{\mathcal{L}}_D)^T$ be the vector of observed LKCs and denote their covariance matrix by $\Sigma = \text{Cov}[\hat{\mathcal{L}}]$. Again changing the order of integration and expectation yields that the (d, d') entries of the covariance matrix Σ can be expressed as

$$(11) \quad \sigma_{dd'} = \text{Cov}[\hat{\mathcal{L}}_d, \hat{\mathcal{L}}_{d'}] = \frac{(2\pi)^{d/2}(2\pi)^{d'/2}}{(d-1)!(d'-1)!} \iint H_{d-1}(u) H_{d'-1}(v) \text{Cov}[\chi(u), \chi(v)] du dv < \infty.$$

using eq. (10). To rigorously prove these statements we require the following assumptions.

- (G1) f is Gaussian and has almost surely \mathcal{C}^2 -sample paths.
- (G2) The distribution of $\left(\frac{\partial f}{\partial s_d}(s), \frac{\partial^2 f}{\partial s_d \partial s_{d'}}(s)\right)$ is nondegenerate for all $s \in S$ and $d, d' = 1, \dots, D$.
- (G3) There is an $\epsilon > 0$ such that

$$\mathbb{E} \left[\left(\frac{\partial^2 f}{\partial s_d \partial s_{d'}}(s) - \frac{\partial^2 f}{\partial s_d \partial s_{d'}}(s') \right)^2 \right] \leq K |\log \|s - s'\||^{-(1+\gamma)}$$

for all $d, d' = 1, \dots, D$ and for all $|s - s'| < \epsilon$. Here $K > 0$ and $\gamma > 0$ are finite constants.

- (G4) $\rho(s, s') = 1$ if and only if $s = s'$, where ρ is the correlation function of f .
- (G5) Let N_f be the number of critical points of f and $\epsilon > 0$.
 - a) $\mathbb{E}[N_f^{1+\epsilon}] < \infty$
 - b) $\mathbb{E}[N_f^{2+\epsilon}] < \infty$

REMARK.

1. (G1)-(G4) are requirements for the validity of the GKF, cf. [2]. Especially, they guarantee that the paths of f are almost surely Morse functions, [2, Chapter 11.3].
2. Assumption (G3) is satisfied for any Gaussian field f having almost surely \mathcal{C}^3 -sample paths, see [37].

3. **(G5)** is sufficient to proof unbiasedness (a) and finiteness of the variance (b) of our estimator. Precise conditions to satisfy these conditions are an active research topic. For $D = 1$ the almost surely $\mathcal{C}^4/\mathcal{C}^7$ -sample paths are sufficient to establish the finiteness of the moments of the number of critical points in **(G5a/b)**, cf. [5, Theorem 3.6]. For $D > 1$ the situation is more complicated. However, for stationary fields weak sufficient conditions have been recently given by [13], which are satisfied for Gaussian fields with \mathcal{C}^3 sample paths.

Note that, if we order the critical values of f by height, then the empirical EC curve $\chi(u)$ is constant between consecutive critical levels. Therefore the estimator (13) can be written as a polynomial function of the critical levels.

THEOREM 1. *Assume f is Gaussian and satisfies **(G1)-(G4)**. Since the paths of f are almost surely Morse functions, we only have finitely many critical values, which we order and denote with $u_0 < \dots < u_M$. Thus,*

$$(12) \quad \chi(u) = \mathcal{L}_0 \mathbb{1}_{(-\infty, u_0]}(u) + \sum_{m=1}^M a_m \mathbb{1}_{(u_{m-1}, u_m]}(u)$$

with random $a_m = \chi(u_m) \in \mathbb{Z}$ and hence

$$\hat{\mathcal{L}}_d = \frac{(2\pi)^{d/2}}{d!} \sum_{m=0}^M (a_m - a_{m+1}) H_d(u_m), \quad \text{with } a_0 = \mathcal{L}_0 \text{ and } a_{M+1} = 0.$$

REMARK. The above representation of $\hat{\mathcal{L}}_d$ is useful for implementation of the estimator, since it shows that we do not need to carry out any numerical integration, which increases accuracy and speeds up the computation.

The next theorem states that the LKC estimators are unbiased and that the covariances are finite under proper assumptions. The strategy of the proofs is identical. We show that Fubini's theorem is applicable, which thereby especially implies that equation (11) is valid and finite. Furthermore, this also means that $\text{Cov}[\chi(u)\chi(u')]$ must decay fast enough, which is stated in the corresponding corollary and gives a partial answer to the widely believed property that the variance $\text{Var}[\chi(u)]$ is decaying exponentially in u .

THEOREM 2. *Assume that f is Gaussian and satisfies **(G1)-(G4)**.*

- a) *If (G5a), then the HPEs are unbiased, i.e., $\mathbb{E}[\hat{\mathcal{L}}_d] = \mathcal{L}_d$.*

b) If (G5b), then the covariances $\sigma_{dd'} = \text{Cov} [\hat{\mathcal{L}}_d, \hat{\mathcal{L}}_{d'}]$ are finite for all $d, d' = 1, \dots, N$.

COROLLARY 1. *Under the assumptions of Theorem 2b) we have that $\text{Cov}[\chi(u)\chi(u')]$ decays faster than any polynomial in u, u' for $u, u' \rightarrow \pm\infty$.*

2.4. Repeated observations. Suppose $f_n(s)$, $s \in S$, $n = 1, \dots, N$, $N \geq 1$, are i.i.d. Gaussian random fields over the domain S with mean 0, variance 1 and unknown covariance function satisfying **(G1)**-**(G4)**.

Let χ_n denote the EC curve of the field f_n . Each χ_n yields a vector of LKC estimates $\hat{\mathcal{L}}_n = (\hat{\mathcal{L}}_{1n}, \dots, \hat{\mathcal{L}}_{Dn})^\top$. Let $\mathcal{L} = (\mathcal{L}_1, \dots, \mathcal{L}_D)^\top$ be the vector of true LKCs. Since the observed LKC vectors are i.i.d., the average estimator

$$(13) \quad \hat{\mathcal{L}}^{(N)} = (\hat{\mathcal{L}}_1^{(N)}, \dots, \hat{\mathcal{L}}_D^{(N)})^\top = \frac{1}{N} \sum_{n=1}^N \hat{\mathcal{L}}_n \xrightarrow{P} \mathcal{L},$$

is seen to be unbiased and consistent as $N \rightarrow \infty$ by the weak law of large numbers (WLLN). Moreover, the vector $\hat{\mathcal{L}}^{(N)}$ has covariance matrix $\text{Cov} [\hat{\mathcal{L}}^{(N)}] = \Sigma/N$ and satisfies a central limit theorem (CLT)

$$(14) \quad \sqrt{N} \left(\hat{\mathcal{L}}^{(N)} - \mathcal{L} \right) \xrightarrow{D} N(0, \Sigma).$$

With repeated observations, the covariance matrix Σ can be estimated unbiasedly and consistently from the data via

$$(15) \quad \hat{\Sigma}^{(N)} = \frac{1}{N-1} \sum_{n=1}^N \left[\hat{\mathcal{L}}_n - \hat{\mathcal{L}}^{(N)} \right] \left[\hat{\mathcal{L}}_n - \hat{\mathcal{L}}^{(N)} \right]^\top.$$

2.5. Parametric estimation of the EEC. Observed LKCs allow smoothing of EC curves as linear combinations of the EC densities via

$$(16) \quad \hat{\chi}_n(u) = \mathcal{L}_0 \Phi^+(u) + \sum_{d=1}^D \hat{\mathcal{L}}_{dn} \rho_d(u)$$

(see Fig. 1). The smooth EC curve has the property that $\text{E}[\hat{\chi}(u)] = \text{EEC}(u)$ so it is an unbiased estimator of the EEC curve. Moreover, since

$$\hat{\chi}_n(u) - \text{E}[\hat{\chi}_n(u)] = \hat{\chi}_n(u) - \text{EEC}(u) = \sum_{d=1}^D (\hat{\mathcal{L}}_{dn} - \mathcal{L}_d) \rho_d(u)$$

from (1), then the covariance function of the smooth EC curve $\hat{\chi}(u)$ is finite and can be expressed as

$$(17) \quad C(u, v) = \text{Cov} [\hat{\chi}_n(u), \hat{\chi}_n(v)] = \sum_{d=1}^D \sum_{d'=1}^D \sigma_{dd'} \rho_d(u) \rho_{d'}(v),$$

where $\sigma_{dd'}$ is the (d, d') entry of the covariance matrix Σ of the observed LKCs given by (11).

With repeated observations, application of (16) with the average observed LKCs yields our proposed HPE of the EEC curve

$$(18) \quad \widehat{\text{EEC}}^{(N)}(u) = \mathcal{L}_0 \Phi^+(u) + \sum_{d=1}^D \hat{\mathcal{L}}_d^{(N)} \rho_d(u).$$

Note that the sum on the right is exactly the projection of the pinned EC curve on the linear space spanned by the EC densities with inner product (6), so just like with the LKCs, this estimator may also be called the *Hermite projection estimator*. By construction, this parametric estimator (parametric in the sense that it depends on estimates of the LKC parameters) is unbiased and pointwise consistent. As shown in Theorem 3 below, it is also uniformly consistent. In Section 2.6 below we consider a nonparametric estimator obtained by averaging the empirical EC curves directly and use simulations later to show that the parametric estimator has lower variance.

By linearity, the parametric, smooth, EEC estimator can also be written and computed as the average of the smoothed EC curves:

$$(19) \quad \widehat{\text{EEC}}^{(N)}(u) = \mathcal{L}_0 \Phi^+(u) + \sum_{d=1}^D \hat{\mathcal{L}}_d^{(N)} \rho_d(u) = \frac{1}{N} \sum_{n=1}^N \hat{\chi}_n(u),$$

where each $\hat{\chi}_n(u)$ is an independent sample of (16), so it has covariance (20)

$$\text{Cov} \left(\widehat{\text{EEC}}^{(N)}(u), \widehat{\text{EEC}}^{(N)}(v) \right) = \frac{1}{N} \text{Cov} [\hat{\chi}_n(u), \hat{\chi}_n(v)] = \frac{1}{N} \sum_{d=1}^D \sum_{d'=1}^D \sigma_{dd'} \rho_d(u) \rho_{d'}(v),$$

by (17). Being an average with finite covariance, the EC density projection estimator satisfies a fCLT. We summarize these properties in the following result.

THEOREM 3. *Under the assumptions (G1)-(G5) the parametric, smooth, estimated EEC curve has the following properties:*

- (i) The estimated EEC curve $\widehat{\text{EEC}}^{(N)}(u)$ and all its derivatives $\frac{d^k}{du^k}\widehat{\text{EEC}}^{(N)}(u)$ for $k \geq 1$ are uniformly consistent estimators of $\text{EEC}(u)$ and its derivatives $\frac{d^k}{du^k}\text{EEC}(u)$, respectively.
- (ii) The estimated EEC curve $\widehat{\text{EEC}}^{(N)}(u)$ satisfies a fCLT so that

$$(21) \quad \sqrt{N} \left[\widehat{\text{EEC}}^{(N)}(u) - \text{EEC}(u) \right] \xrightarrow{N \rightarrow \infty} G(u) = \sum_{d=1}^D Z_d \rho_d(u)$$

weakly as a stochastic process in $C(\mathbb{R})$, where Z_1, \dots, Z_D are Gaussian variables with mean zero and covariance Σ , as in (14).

Note that $G(u)$ in (21) is a smooth Gaussian random field with mean zero and covariance function $C(u, v)$ (17). Again, the constants $\sigma_{dd'}$ can be estimated using (15). This result is remarkable because it does not require knowledge of the covariance function of the EC curves $\chi_n(u)$ themselves. Unlike the EEC (1), a similar expression for the covariance function for all u is unknown. Here it is only known that the covariance must decay faster than any polynomial, cf Corollary 1.

The CLT allows constructing confidence regions for the EEC curve. In particular, asymptotic two-sided $1 - \alpha$ pointwise confidence bands can be built as

$$(22) \quad \widehat{\text{EEC}}^{(N)}(u) \pm z_{1-\alpha/2} \sqrt{\hat{C}(u, u)/N},$$

where the estimate of the variance function $\hat{C}(u, u)$ is obtained as a plug-in estimator substituting the sample covariance $\hat{\Sigma}$ in (17) and $z_{1-\alpha/2}$ is the $1 - \alpha/2$ quantile of the standard normal distribution.

REMARK. Using the GKF or the multiplier-t bootstrap for the normalized limiting process $G(u)$ in (21), it is possible to even provide for any compact set $U \subset \mathbb{R}$ asymptotic simultaneous confidence bands for $\text{EEC}(u)$ constructed as in [37].

2.6. *Nonparametric estimation of the EEC.* As a point of comparison, we consider a nonparametric alternative to estimation of the EEC. Given the observed EC curves $\chi_n(u)$, $n = 1, \dots, N$, it is natural to estimate the EEC nonparametrically by the average

$$(23) \quad \bar{\chi}^{(N)}(u) = \frac{1}{N} \sum_{n=1}^N \chi_n(u).$$

Since the observed EC curves are i.i.d. and have finite variance under **(G5b)**, (23) is also unbiased and consistent as an estimator of the EEC and satisfies the CLT

$$(24) \quad \sqrt{N} \left[\bar{\chi}^{(N)}(u) - \text{EEC}(u) \right] \xrightarrow{D} W(u)$$

pointwise for each $u \in \mathbb{R}$, where $W(u)$ is a centered Gaussian variable with variance $\text{Var}[\chi(u)]$. Based on the CLT, pointwise confidence intervals based on the EC average estimator can be constructed as

$$(25) \quad \bar{\chi}^{(N)}(u) \pm z_{1-\alpha/2} \sqrt{\widehat{\text{Var}}[\chi(u)]/n},$$

where $\widehat{\text{Var}}[\chi(u)]$ is the sample variance of $\chi_1(u), \dots, \chi_n(u)$.

REMARK. By the linearity of the Hermite projection (10), the HPE (13) can be equivalently obtained from the average EC curve (23), using the projection (8), as

$$(26) \quad \hat{\mathcal{L}}_d^{(N)} = \frac{\langle \bar{\chi}^\circ, \rho_d \rangle}{|\rho_d|^2} = \mathcal{H}_d\{\bar{\chi}^\circ\} = \mathcal{H}_d\{\bar{\chi}^{(N)}(u) - \mathcal{L}_0\Phi^+(u)\}.$$

Thus, the HPE of (18) is a linear function of $\bar{\chi}(u)$. In fact, it is the orthogonal projection of $\bar{\chi}(u)$ onto the vector space spanned by the EC densities according to the inner product (6).

2.7. *LKC estimation for asymptotically Gaussian fields.* The previously developed theory relies on the assumption that the observed samples from f are mean zero constant variance Gaussian fields. None of that is usually known in applications. However, often only the EEC curve of a limiting field obtained from a fCLT is of interest for inference, e.g., [42, 33].

We here describe how to apply the previously introduced method in this setting. Firstly, assume there exist a sequence $\tau_N \in \mathbb{R}_+$ and a continuous function $\sigma : S \rightarrow \mathbb{R}_+$ bounded from above and below such that

$$(27) \quad \tau_N \frac{\hat{\mu}_N(s) - \mu(s)}{\sigma(s)} \xrightarrow{N \rightarrow \infty} \mathcal{G}(s),$$

weakly in $C(S)$, where \mathcal{G} is a mean zero, unit variance Gaussian field with covariance \mathfrak{r} satisfying **(G1)**-**(G4)**. Since \mathcal{G} by assumption satisfies the GKF, our goal becomes estimating its EEC using the HPE.

Sampling from the Limiting Field. The challenge is estimation of the LKCs of the limiting field \mathcal{G} . In order to do that we need sample fields from the limiting Gaussian field, which can be used in the HPE (10).

As a motivation for why the samples f_1, \dots, f_N cannot be immediately used in the HPE, assume for example they are an iid sample of a Gaussian field f with unknown mean and variance function. Note that the sample mean $\hat{\mu} = \bar{f}$ satisfies the fCLT (27) with \mathcal{G} having the correlation structure of f as covariance structure. However, the f_n 's despite being Gaussian cannot be directly used for estimation of the LKCs, since they are neither constant mean zero nor constant variance. Moreover, the standardized residuals

$$(28) \quad R_n^N = \frac{f_n - \bar{f}}{\sqrt{N^{-1} \sum_{n=1}^N (f_n - \bar{f})^2}}$$

are not Gaussian and therefore cannot be used as input into the HPE either.

Thus, we aim to generate Gaussian sample fields having properties close to the limiting Gaussian field \mathcal{G} by using the Gaussian multiplier bootstrap on a set of residuals.

DEFINITION 1 (Residuals for fCLT). For all $N \in \mathbb{N}$ let $R_1^N, \dots, R_N^N \sim R^N$ be identical distributed random fields such that $\mathbb{E}[R^N] = 0$ and such that the empirical correlation function

$$(29) \quad \hat{\mathbf{r}}(s, s') = \frac{\sum_{n=1}^N R_n^N(s) R_n^N(s')}{\sqrt{\sum_{n=1}^N (R_n^N(s))^2} \sqrt{\sum_{n=1}^N (R_n^N(s'))^2}} \xrightarrow{a.s.} \mathbf{r}(s, s')$$

pointwise almost surely as $N \rightarrow \infty$. Then we call the samples R_1^N, \dots, R_N^N a set of residuals for the fCLT (27).

DEFINITION 2 (AGMBF). Given a set of residuals R_1^N, \dots, R_N^N for the fCLT (27). We define the associated Gaussian multiplier bootstrap field (AGMBF) by

$$(30) \quad R_N^{*,g} = \frac{\sum_{n=1}^N g_n R_n^N}{\sqrt{\sum_{n=1}^N (R_n^N)^2}}, \quad \text{with } g_1, \dots, g_n \sim N(0, 1),$$

where the g_n 's are mutually independent.

Note, that $\mathbb{E}[R_N^{*,g}(s)] = 0$ and $\mathbb{E}[R_N^{*,g}(s) R_N^{*,g}(s')] = \hat{\mathbf{r}}(s, s')$ for all $s, s' \in S$ and hence samples from the Gaussian process $R_N^{*,g}$ approximate the samples of \mathcal{G} by having the empirical correlation structure of the residuals.

Estimation of the LKCs. Assuming that the AGMBF $R_N^{*,g}$ satisfies **(G1)**-**(G5)** the SLLN and Theorem 4 imply that for an independent bootstrap sample $R_N^{*,g_1}, \dots, R_N^{*,g_M} \sim R_N^{*,g}$ we have that

$$(31) \quad \hat{\mathcal{L}}^B = \frac{1}{M} \sum_{m=1}^M \hat{\mathcal{L}}(R_N^{*,g_m}) \xrightarrow{a.s.} \mathcal{L}(R_N^{*,g}).$$

We call this estimator the *bootstrap Hermite projection estimator* (bHPE) and use it to estimate the LKCs $\mathcal{L}(\mathcal{G})$ of the limiting process \mathcal{G} in (27) from a given set of residuals.

Note that by (31) the bHPE up to bootstrap sampling gives the LKCs of the Gaussian field with the empirical correlation structure of the residuals and therefore computes exactly the same quantity as targeted in the WarpE method [36].

Consistency of the bHPE. We now theoretically justify that the bHPE is consistent for estimation of the LKCs of the limiting field of the estimator $\hat{\mu}_N(s)$. The following conditions are required.

- (R1)** The AGMBF $R_N^{*,g}$ satisfies **(G1)**-**(G5)** for almost all sets of residuals R_1^N, \dots, R_N^N .
- (R2)** The empirical correlation $\hat{\mathbf{t}}$ in (29) and its partial derivatives up to order 2 converge uniformly almost surely to \mathbf{t} and its partial derivatives, respectively.

REMARK. **(R1)** lists the conditions so that Theorem 2 can be applied to $R_N^{*,g}$. **(G1)** and **(G3)** are true, e.g., if the residual field R^N has almost surely C^3 sample paths for all $N \in \mathbb{N}$, cf., [37, Remark 3]. **(G2)** translates into a condition on full rank of a sample covariance of partial derivatives of $R_N^{*,g}$, which by the Cauchy-Schwarz inequality can be equivalently written as

$$\mathbb{P} \left(\forall s \in S \exists n, n' \in \{1, \dots, N\} \forall \lambda \in \mathbb{R} : \left(\frac{\partial \tilde{R}_n^N}{\partial s_d}(s), \frac{\partial \tilde{R}_{n'}^N}{\partial s_d}(s) \right) \neq \lambda \left(\frac{\partial \tilde{R}_n^N}{\partial s_d \partial s_{d'}}(s), \frac{\partial \tilde{R}_{n'}^N}{\partial s_d \partial s_{d'}}(s) \right) \right) = 1,$$

where $\tilde{R}_{n'}^N = R_{n'}^N / \sqrt{\sum_{n=1}^N (R_n^N)^2}$, for all $N \in \mathbb{N}$, $N > 2$, and for all $d, d' \in \{1, \dots, D\}$. A similar argument can be applied to restate **(G4)** into:

$$\mathbb{P} \left(\forall s, s' \in S \exists n, n' \in \{1, \dots, N\} \forall \lambda \in \mathbb{R} : \left(R_n^N(s), R_{n'}^N(s) \right) \neq \lambda \left(R_n^N(s'), R_{n'}^N(s') \right) \right) = 1$$

for all $N \in \mathbb{N}$, $N > 2$, for all $d, d' \in \{1, \dots, D\}$.

A tractable condition to ensure **(R2)** is given by L^2 -Lipschitz continuity of the residual field R^N and all its partial derivatives up to order 2, cf., [37, Lemma 3].

THEOREM 4.

1. Given a set of residuals R_1, \dots, R_N the AGMBF $R_N^{*,g}$ is mean zero, unit variance Gaussian with $E[f^{*,g}(s)f^{*,g}(s')] = \hat{\tau}(s, s')$.
2. Assume **(R1)**, then $\hat{\mathcal{L}}^B \xrightarrow{a.s.} \mathcal{L}(R_N^{*,g})$ as $M \rightarrow \infty$.
3. Assume additionally **(R2)**, then $\mathcal{L}(R_N^{*,g}) \xrightarrow{a.s.} \mathcal{L}(\mathcal{G}(0, \mathbf{r}))$ as $N \rightarrow \infty$.

3. Extensions.

3.1. *Inference based on the estimated EEC.* The EEC curve is often used in inference for images. For example, it is often of interest to find a significance threshold u_α such that $EEC(u_\alpha) = \alpha$. For very high thresholds u , [35] showed that

$$EEC(u) \approx P \left\{ \sup_{s \in S} f_n(s) > u \right\}.$$

Thus choosing the threshold u_α permits controlling the FWER of the excursion set $A_n(u_\alpha)$ where the field $f_n(t)$ exceeds the threshold u_α . This was the pioneering approach taken by Keith Worsley in the analysis of brain images, typically with $\alpha = 0.05$ [39, 42].

In this paper we consider an additional interpretation. For high but somewhat lower thresholds, the EEC curve counts the expected number of connected components in $A_n(u)$, and so the threshold u_α controls the expected number of connected components to be below α . Although uncommon, this thresholding strategy has been used in neuroimaging as well with $\alpha = 1$ [6], so that thresholding at u_1 produces one false connected component of the excursion set, in expectation.

Suppose now that the EEC curve is estimated via (18) and a significance threshold $\hat{u}_\alpha^{(N)}$ is found that satisfies $\widehat{EEC}^{(N)}(\hat{u}_\alpha^{(N)}) = \alpha$. We wish to know how variable is this threshold.

THEOREM 5. *The random threshold $\hat{u}_\alpha^{(N)}$ has the following properties:*

- (i) $\hat{u}_\alpha^{(N)}$ is a consistent estimator of u_α .
- (ii) Let α be small enough such that $g'(u_\alpha) \neq 0$. Then $\sqrt{N} \left(\hat{u}_\alpha^{(N)} - u_\alpha \right)$ converges in distribution to $G(u_0)/g'(u_0)$.

$$(32) \quad \sqrt{N} \left(\hat{u}_\alpha^{(N)} - u_\alpha \right) \xrightarrow{D} \frac{G(u_\alpha)}{\tau(u_\alpha)},$$

where $G(u)$ is the Gaussian process in (21) and $\tau(u)$ is the derivative of the EEC curve

$$\tau(u) = \text{EEC}'(u) = \sum_{d=0}^D \mathcal{L}_d \rho_d'(u) = \sqrt{2\pi} \sum_{d=0}^D \mathcal{L}_d \rho_{d+1}(u).$$

A consequence of Theorem 5 is that, for large N , \hat{u}_α is approximately Gaussian with mean u_α and variance

$$(33) \quad \text{Var} \left[\hat{u}_\alpha^{(N)} \right] = \frac{C(u_\alpha, u_\alpha)}{N\tau^2(u_\alpha)},$$

where $C(u, u)$ is given by (17). In practice, we estimate this variance by substituting estimators for u_α , $C(u, u)$ and the LKCs as described above.

3.2. EEC estimation for pointwise linear models. For fMRI data in particular [39, 42, 23], but also in other settings [33], it is customary to set up a linear regression model relating the observed random fields at each location s . Following what is usually called the general linear model (GLM) approach, the $n \times 1$ vector $\mathbf{Y}(s)$ of observed intensities at each location s is modeled as

$$(34) \quad \mathbf{Y}(s) = \mathbf{X}\boldsymbol{\beta}(s) + \boldsymbol{\epsilon}(s),$$

where the $p \times 1$ vector $\boldsymbol{\beta}(s)$ contains p regression coefficients, \mathbf{X} is a constant $N \times p$ design matrix independent of s , and $\boldsymbol{\epsilon}(s)$ is a $N \times 1$ random vector whose entries are assumed to be i.i.d. with zero mean and some variance $\sigma^2(s)$. In a task-related fMRI experiment, $\mathbf{Y}(s)$ represents the observed fMRI images at N time points and \mathbf{X} contains the onset of the various task conditions in addition to other covariates, so that the function $\boldsymbol{\beta}(s)$ represents the extent to which the observed signal is related to the task at each location s . The goal of the inference is to estimate a specific contrast $\eta(s) = \mathbf{c}'\boldsymbol{\beta}$, for a fixed vector \mathbf{c} , typically comparing task conditions. The detection of regions of activation in relation to the contrast corresponds to thresholding a standardized estimate of $\eta(s)$, so that the error is controlled as described in Section 3.1.

Specifically, let $\hat{\boldsymbol{\beta}}(s) = (\mathbf{X}'\mathbf{X})^{-1}\mathbf{X}'\mathbf{Y}(s)$ be the usual pointwise least-squares estimate of the coefficient vector $\boldsymbol{\beta}(s)$ at each location s , with covariance matrix $\text{Cov}[\hat{\boldsymbol{\beta}}(s)] = \sigma^2(s)(\mathbf{X}'\mathbf{X})^{-1}$. The estimate of $\eta(s)$ is $\hat{\eta}(s) = \mathbf{c}'\hat{\boldsymbol{\beta}}(s)$, with variance $\text{Var}[\hat{\eta}(s)] = \sigma^2(s)\mathbf{c}'(\mathbf{X}'\mathbf{X})^{-1}\mathbf{c}$. Inference at each location s , for example to test the null hypothesis $H_0 : \eta(s) = 0$ at each location

s , may be based on the standardized z-score field

$$(35) \quad z(s) = \frac{\hat{\eta}(s)}{\sqrt{\text{Var}[\hat{\eta}(s)]}}.$$

Let $\rho(s, t) = \text{E}[\epsilon_n(s), \epsilon_n(t)]$, $s, t \in S$, be the correlation function of the noise field. A simple calculation shows that the random field $z(s)$ has constant variance 1 and covariance function equal to $\rho(s, t)$. Under the complete null hypothesis that $H_0 : \eta(s) = 0$ for all $s \in S$, the random field $z(s)$ also has zero mean. As in Section 3.1, the detection threshold u_α can be obtained as the point where the EEC of $z(s)$ equals α .

If the error field ϵ is smooth and the design matrix is appropriately bounded [33], then the z-score field (35) satisfies a fCLT with a smooth Gaussian limiting field and its EEC obeys the GKF (1), with the LKCs being the same as those of the error field ϵ .

Ideally, the estimation procedure of Section 2.5 would be applied to N i.i.d. instances of the error field. Since these are not available, we may proceed as in [36] and use the residual fields contained in the vector $\mathbf{e}(s) = \mathbf{Y}(s) - \mathbf{X}\hat{\boldsymbol{\beta}}(s)$ instead. The normalized residual field vector $\tilde{\mathbf{e}}(s) = \mathbf{e}(s)/\sigma(s)$ is smooth and has mean zero and covariance function $\text{E}[\tilde{\mathbf{e}}(s)\tilde{\mathbf{e}}'(t)] = [\mathbf{I} - \mathbf{X}(\mathbf{X}'\mathbf{X})^{-1}\mathbf{X}']\rho(s, t)$. While these fields are not independent, classical results in linear regression (e.g. [11]) indicate that asymptotic properties still hold if the sample size N is replaced by the number of degrees of freedom $N - P$. For large N , the variance estimate $\hat{\sigma}^2(s) = \|\mathbf{e}(s)\|^2/(N - P)$ should be close to its true value. Since the normalized residuals are not observable we base our estimates on the standardized residual fields, i.e. the entries of $\hat{\mathbf{e}}(s) = \mathbf{e}(s)/\hat{\sigma}(s)$. Note that even if the error field ϵ is Gaussian, the standardized residual fields $\hat{\mathbf{e}}$ are not. For this reason, the bHPE from Section 2.7 works better than the HPE estimator from Section 2.2, as we will see in the simulations below.

4. Simulated examples.

4.1. *Design of the Simulations.* In the following sections we compare the performance of the Hermite projection estimator (HPE) given by (13), the bootstrapped Hermite projection estimator (bHPE) from (31), the warping-to-isotropy estimator (WarpE), c.f. [41], [36] and an estimator (IsotE) tailored specifically to isotropic fields with the square exponential covariance function, c.f. [40] and [19]. The latter is implemented in the software package SPM, which is often used in statistical analysis of neuroimage data. If not stated otherwise, the number of Monte Carlo simulations is 1000.

We consider two different scenarios. In the *theoretical scenario*, we assume that the mean and variance are known as required for the theory presented in Sections 2.1-2.4, and generate zero-mean and unit variance fields to estimate the LKC. In the *experimental scenario*, we assume that the mean and variance are unknown and thus use the standardized residuals as input for the estimators instead of directly using the generated samples.

4.2. *Isotropic Gaussian and non-Gaussian 2D fields.* A common example of an isotropic random field is

$$(36) \quad f(s) = \frac{1}{\sqrt{\pi\nu}} \iint e^{-\frac{\|s-t\|^2}{2\nu^2}} W(dt), \text{ for } s \in [1, L]^2,$$

where the W is a Wiener field (white noise) on \mathbb{R}^2 . Note that $\text{Var}[f(s)] = 1$ and the covariance function of $f(s)$ is $C(s) = e^{-\beta\|t\|^2}$ with $\beta = 1/(4\nu^2)$.

For an isotropic field f restricted to a domain $S \subset \mathbb{R}^2$, its LKCs are given by $\mathcal{L}_0 = \mathcal{L}_0(S)$, $\mathcal{L}_1 = \lambda_2^{1/2} \mathcal{L}_1(S)$ and $\mathcal{L}_2 = \lambda_2 \mathcal{L}_2(S)$, where $\mathcal{L}_0(S)$, $\mathcal{L}_1(S)$, and $\mathcal{L}_2(S)$ are the LKCs of the domain S and λ_2 is the second spectral moment, equal to the variance of any directional derivative of f or to the second derivative of the covariance function at the origin [2]. In particular, for a square domain of side L simulated on a discrete grid $\{1, \dots, L\}^2$, the LKCs of the square $S = [1, L]^2$ are 1 (the EC of the square), $2(L-1)$ (half the length of the boundary) and $(L-1)^2$ (volume of the domain), respectively. For the fields (36), it is easy to check that $\lambda_2 = C''(0) = 2\beta$, yielding $\mathcal{L}_0 = 1$, $\mathcal{L}_1 = 2\sqrt{2\beta}(L-1)$ and $\mathcal{L}_2 = 2\beta(L-1)^2$.

Since we cannot generate random i.i.d. fields $f_1(s), \dots, f_N(s)$ directly from the above integral, we instead approximate the process (36) using a discrete convolution, i.e.,

$$(37) \quad f_n(s) = \frac{\sum_{k,l=1}^L e^{-\frac{\|s-(k,l)\|^2}{2\nu^2}} W_{kl;n}}{\sum_{k,l=1}^L e^{-\frac{\|s-(k,l)\|^2}{\nu^2}}},$$

where $W_{kl;n}$, $k, l = 1, \dots, L$, $n = 1, \dots, N$ are i.i.d. random variables with mean 0 and variance 1. We consider a Gaussian case, where each of these variables is $N(0, 1)$ and a non-Gaussian case where each variable is $(\chi_3^2 - 3)/\sqrt{6}$.

Numerically, to prevent boundary effects, we applied the convolution to random $(L + \lceil 4\nu \rceil) \times (L + \lceil 4\nu \rceil)$ -matrices and used only the inner $L \times L$ -matrices as samples of the random field. Note that the LKCs for the Gaussian and the non-Gaussian version of the fields (37), if ν is large enough, can be approximated by the LKCs of the field (36).

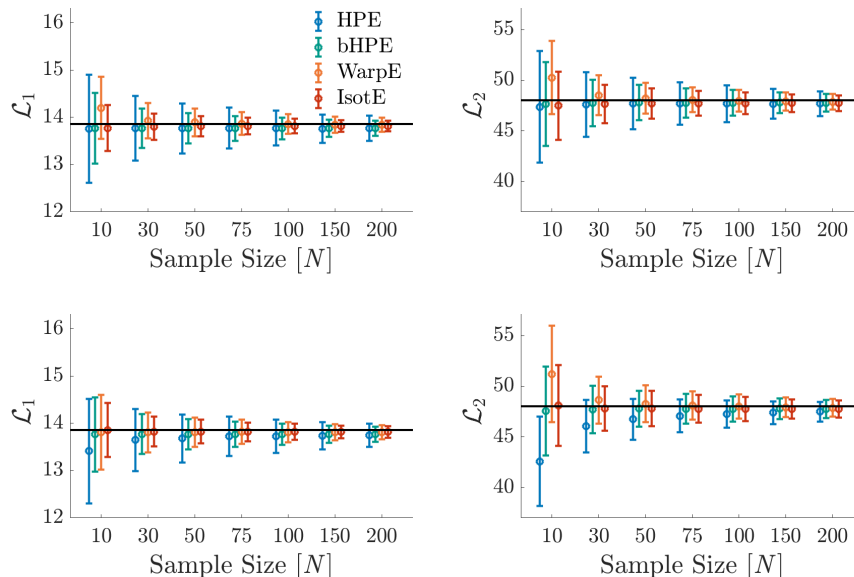


FIG 2. *Isotropic Gaussian field example: estimation accuracy of different estimators $\mathcal{L}_1^{(N)}$ (left) and $\mathcal{L}_2^{(N)}$ (right). Each “o” and its corresponding line mark the average and standard deviation of the estimates based on 1000 simulations. Black lines represent the true LKCs ($\mathcal{L}_1 = 13.86$ and $\mathcal{L}_2 = 48.02$). Theoretical scenario (Top row). Experimental scenario (Bottom row).*

As illustration, Figure 1(top left) shows a single realization of the Gaussian version of the field defined in (37) for $\nu = 5$ and $L = 50$. For this value of ν , $\beta = 0.01$ and so $\mathcal{L}_1 = 13.86$ and $\mathcal{L}_2 = 48.02$. The observed EC curve $\chi_n(u)$ for this particular instance of the field is shown in Figure 1(top right). Smoothing it via (16) produces the superimposed $\hat{\chi}_n(u)$ curve in blue.

To illustrate the estimation procedure, Figure 1(bottom left) shows the EC curves $\chi_n(u)$ corresponding to $N = 10$ i.i.d. replicates of the field. Direct average of the EC curves gives the nonparametric estimate $\bar{\chi}(u)$ in blue. Smoothing via (16) produces the $\hat{\chi}_n(u)$ curves in Figure 1(bottom right). Their average, equal to $\widehat{\text{EEC}}(u)$, is closer to the true EEC curve in red.

LKC estimation. In the Gaussian case, Figure 2 confirms the theoretical results that the HPE and the bHPE are consistent in the theoretical scenario. For every N , HPE is almost unbiased in the theoretical scenario, as predicted by Theorem 2 a), but bHPE is almost unbiased in both the theoretical and experimental scenarios. Moreover, the bHPE has a better variance than the HPE, which is comparable to the variance of the warping estimator. Note in particular that also the standard error bars in the estimation decay as

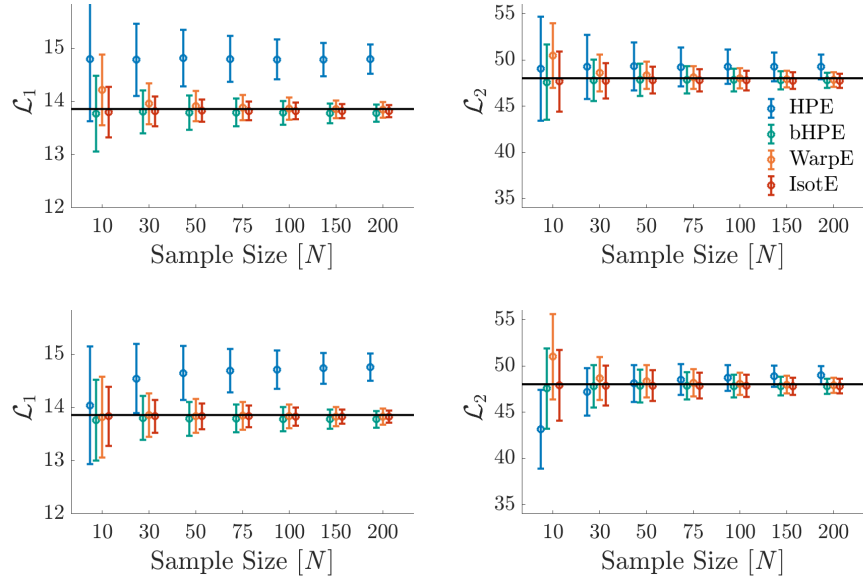


FIG 3. *Isotropic non-Gaussian field example: estimation accuracy of different estimators $\mathcal{L}_1^{(N)}$ (left) and $\mathcal{L}_2^{(N)}$ (right). Each “o” and its corresponding line mark the average and standard deviation of the estimates based on 1000 simulations. Black lines represent the true LKCs ($\mathcal{L}_1 = 13.86$ and $\mathcal{L}_2 = 48.02$). Theoretical scenario (Top row). Experimental scenario (Bottom row).*

$1/\sqrt{N}$, as predicted by the theory.

For non-Gaussian data, Figure 3 shows that the bHPE still works and performs better than the warping estimator. Moreover, its performance is almost the same as that of the isotropic estimator, even though it does not know that the field is isotropic.

In the simulations above, all the estimators have a very small downward asymptotic bias that does not go away as N increases. To elucidate this, Table 1 shows the relative difference between the LKC estimates of the HPE of (37) and the theoretical LKCs of (36) in the Gaussian theoretical scenario. This difference vanishes as ν increases, which indicates that the small asymptotic bias is due to the discrete approximation of the field (36). The same is true for the other scenarios (results not shown).

EEC estimation. Moving on to the estimation of the EEC curve, the covariance function (20) of the EEC curve estimates $\widehat{\text{EEC}}(u)$ and $\bar{\chi}(u)$ for a sample size of $N = 10$ based on 1000 simulations are shown as images in Figure 4. Taking the diagonal entries gives the variance function, which in turn allows constructing the pointwise confidence bands shown in Figure

ν	2	3	5	6	7
$\widehat{\mathcal{L}}_1, N = 10$	-0.0195	-0.0179	-0.0075	-0.0025	0.0011
$\widehat{\mathcal{L}}_2, N = 10$	-0.0169	-0.0090	-0.0097	-0.0069	0.0045
$\widehat{\mathcal{L}}_1, N = 75$	-0.0240	-0.0121	-0.0075	-0.0047	0.0012
$\widehat{\mathcal{L}}_2, N = 75$	-0.0138	-0.0076	-0.0065	-0.0065	0.0006

TABLE 1

Relative bias $E[\widehat{\mathcal{L}}_i - \mathcal{L}_i]/\mathcal{L}_i$ depending on the sample size N and bandwidth ν for the HPE. For large ν the bias decreases, which suggests that the bias in our LKC estimates is primarily due to the discrete approximation (37) of the isotropic field (36), since the approximation improves for larger ν .

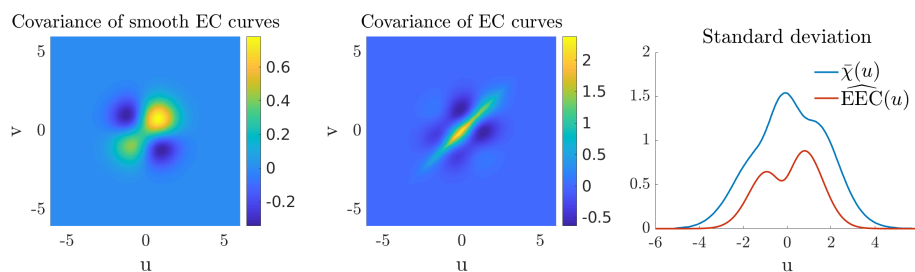


FIG 4. Isotropic Gaussian field example: covariance functions of the parametric EEC curve estimator $\widehat{EEC}(u)$ (20) (left) and the nonparametric EC average curve $\bar{\chi}(u)$ (23) (middle) for $N = 100$ based on 1000 simulations. The right panel shows the standard deviation functions of $\widehat{EEC}(u)$ (red) and $\bar{\chi}(u)$ (blue).

1(bottom row). Note that the parametric EEC estimator has lower variance than the nonparametric estimator (right panel).

Figure 5 shows simulation results (1000 repetitions) for the coverage of the true EEC curves when constructing pointwise 95% confidence intervals via (22) and (25) for the HPE and EC average estimators, respectively. In the top row, the CIs use the “true” variance of the EC curves, estimated by Monte Carlo simulation for a large sample size of 10000, while in the bottom row, the CIs use the variance estimates corresponding to the given sample size. It can be seen that the coverage function is not only smoother for the HPE (red), but it guarantees coverage for extreme values of u especially when the variance is estimated from the data, while for the EC average coverage is lost due to non-existent observations.

4.3. *2D scale-space non-stationary Gaussian field.* Let the i.i.d. random fields be generated via

$$f_n(t, \gamma) = \frac{1}{\pi^{1/4} \sqrt{\gamma}} \int e^{-\frac{(t-s)^2}{2\gamma^2}} W_n(ds), \quad n = 1, \dots, N,$$

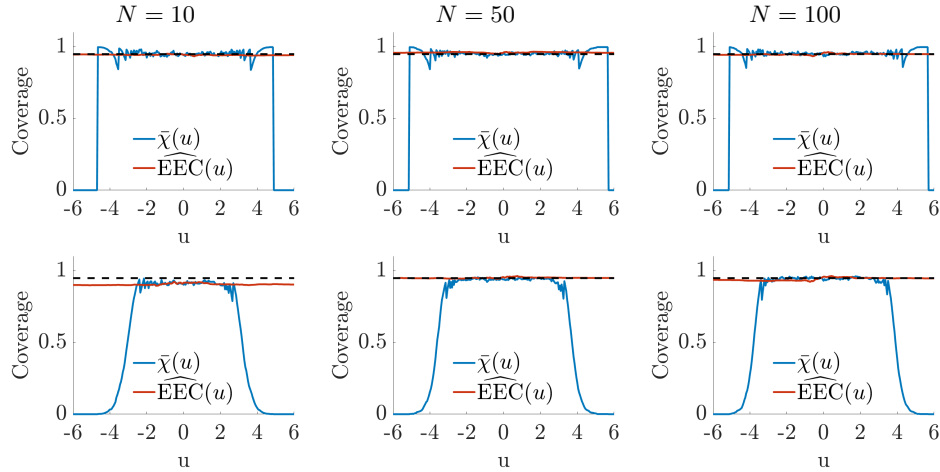


FIG 5. *Isotropic Gaussian field example: simulated pointwise coverage of the EEC curve under respectively “true” variance of the EC curves (top row) and estimated variance (bottom row) for the given sample size. Red lines and blue lines are respectively simulated coverage rates for $\widehat{\text{EEC}}(u)$ and $\bar{\chi}(u)$. The dashed lines represent the target confidence level 95%.*

where $t \in \mathbb{R}$, $\gamma \in (0, \infty)$ and the W_n 's are i.i.d. Wiener fields (white noise) on \mathbb{R} , so that $\text{Var}[f_n(t, \gamma)] = 1$. These are unit-variance, smooth, non-stationary Gaussian random fields over $\mathbb{R} \times (0, \infty)$ and are called *scale space fields*. Suppose the domain is $[1, L] \times [\gamma_1, \gamma_2]$. Then, by [32],

$$\begin{aligned} \mathcal{L}_1 &= \frac{L-1}{2} (\gamma_1^{-1} + \gamma_2^{-1}) \sqrt{\lambda} + \sqrt{\kappa} \log(\gamma_2/\gamma_1), \\ \mathcal{L}_2 &= (L-1) (\gamma_1^{-1} - \gamma_2^{-1}) \sqrt{\lambda\kappa}, \end{aligned}$$

where

$$\lambda = \frac{1}{\sqrt{\pi}} \int s^2 e^{-s^2} ds = \frac{1}{2}, \quad \kappa = \frac{1}{\sqrt{\pi}} \int \left(\frac{1}{2} - s^2\right)^2 e^{-s^2} ds = \frac{1}{2}.$$

In the simulations we again replaced the continuous process by a version derived from a discrete convolution using the parameters $L = 50$, $\gamma_1 = 4$ and $\gamma_2 = 15$. This yields theoretical LKC values of $\mathcal{L}_1 = 6.42$ and $\mathcal{L}_2 = 4.49$. Figures 7 through 9 show the results for the scale space following the same format as Figures 2 through 5 with 1000 repetitions. These results show that the same properties shown in the isotropic case also hold for this non-stationary field. In particular, the bHPE and WarpE are the best and perform similarly. The IsotE, which is the only estimator currently used in neuroimaging, is unsuitable under strong nonstationarity.

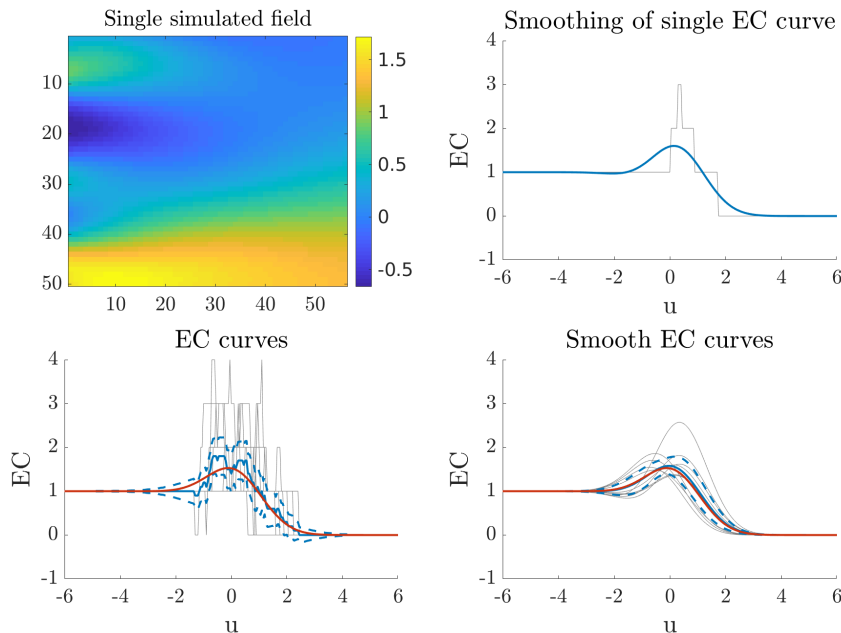


FIG 6. (Top left) A single realization of a scale space produced as convolution of white noise with a Gaussian kernel. (Top right) The corresponding empirical EC curve (gray) and smoothed EC curve (blue). (Bottom left) EC curves (gray) for $N = 10$ realizations of the field and their average (blue). (Bottom right) The corresponding smoothed EC curves (gray) and their pointwise average (blue), which is the estimated EEC curve. The dashed blue lines are pointwise 95% confidence bands for the true EEC curve. In both bottom panels, the true EEC curve is superimposed in red.

5. Applications.

5.1. *fMRI: Nonstationary 3D random field.* In fMRI analysis, the use of random field theory for controlling FWER has been mostly restricted to calculations based on stationarity of the error field, in particular assuming a Gaussian autocorrelation function. In this example, we show how the methods proposed in this paper can be used to obtain the significance threshold without assuming stationarity and taking into account the variability in the EEC estimation.

The fMRI data [22], obtained from the public repository OpenfMRI (openfmri.org), is the same analyzed in [7], allowing us to compare the results. The dataset involves a “false belief task” experiment, where subjects read short stories concerning a person’s false belief about reality or stories about false realities not involving people. The goal of the analysis is to find brain regions that

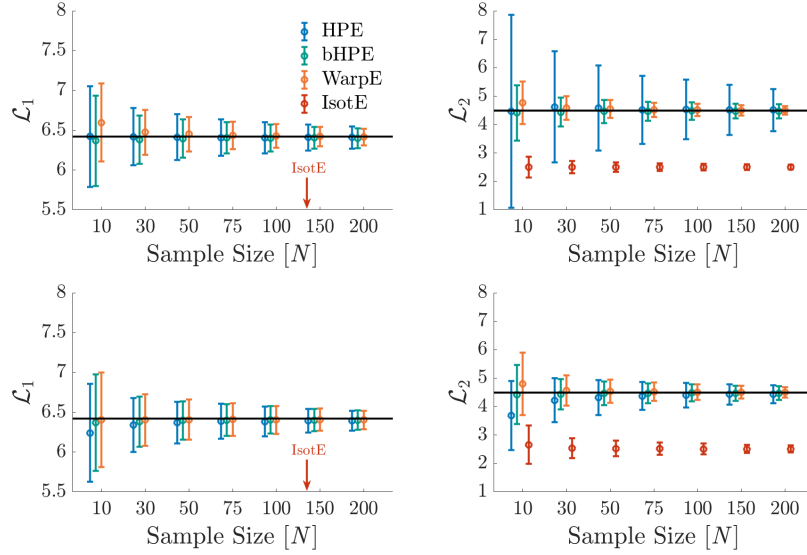


FIG 7. *Scale space field example: estimation accuracy of different estimators $\mathcal{L}_1^{(N)}$ (left) and $\mathcal{L}_2^{(N)}$ (right) as a function of the sample size N . Each “o” its corresponding line mark the average and standard deviation of the estimates based on 1000 simulations. Black lines represent the true LKCs ($\mathcal{L}_1 = 6.42$ and $\mathcal{L}_2 = 4.49$). The values for the IsotE [40] for \mathcal{L}_1 are not shown, since they are far off ($\hat{\mathcal{L}}_1 \approx 3.16$). Theoretical scenario (Top row). Experimental scenario (Bottom row).*

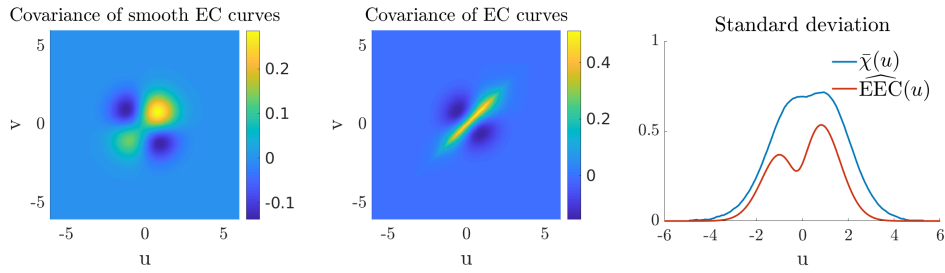


FIG 8. *Scale space example: covariance functions of the HPE EEC estimate $\widehat{\text{EEC}}(u)$ (20) (left) and the EC average $\bar{\chi}(u)$ (23) (middle) for $N = 10$. The right panel shows the variance functions of $\widehat{\text{EEC}}(u)$ (red) and $\bar{\chi}(u)$ (blue).*

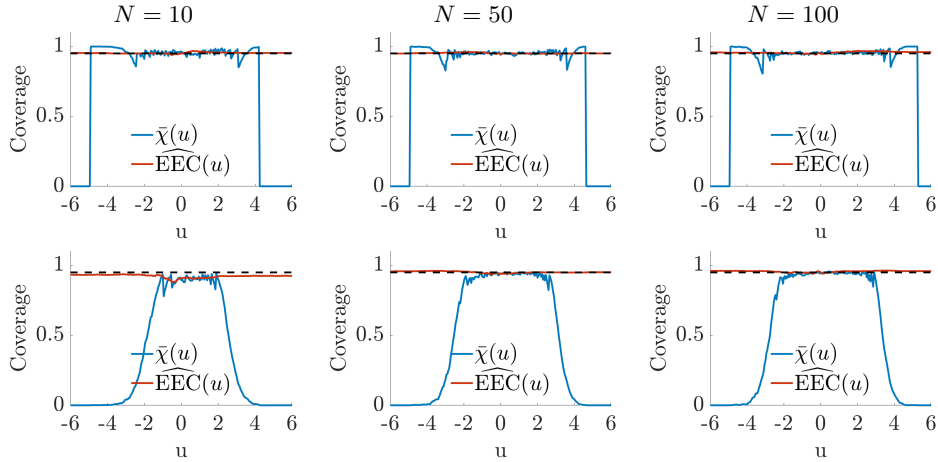


FIG 9. *Scale space example: simulated pointwise coverage of the EEC curve under respectively “true” variance (top row) and estimated variance (bottom row) for the given sample size. Red lines and blue lines are respectively simulated coverage rates for $\widehat{\text{EEC}}(u)$ and $\bar{\chi}(u)$. The dashed lines represent the target confidence level 95%.*

show a contrast in neural activity between these two situations, and can thus be attributed to processing other people’s false beliefs about reality.

As in [7], we focus here on the data from subject # 49. The data $\mathbf{Y}(s)$ consists of a sequence of $N = 179$ fMRI images of size $71 \times 72 \times 36$ voxels, after motion correction, spatial registration and removal of the first row (missing data). The design matrix \mathbf{X} contains 4 columns encoding the presentation of the stimuli as 0-1 step functions, in addition to a column for the intercept term. The vector \mathbf{c} encodes the contrast of interest between the two types of stimuli. Following the analysis described in Section 3.2, we computed the regression residual fields $\mathbf{e}_i(s)$, which we smoothed with a Gaussian kernel with standard deviation of 1.6 voxels and the corresponding z-score field $z(s)$ from equation (35).

To compute EC curves, the spatial domain S was defined as a brain mask composed of all voxels with raw fMRI activity greater than 500. Figure 10 shows the observed and smoothed EC curves for the $N = 179$ re-normalized residual fields restricted to the brain mask S , together with the nonparametric and smooth EEC estimates. As expected, the smooth EEC estimate has tighter confidence bands. To perform statistical inference, we proceed as in Section 3.1. The results are summarized in Table 2. Here u_{FW} and u_{C} are the detection thresholds corresponding to $\alpha = 0.05$ and $\alpha = 1$, respectively. Note also that we only provide standard errors for the LKCs

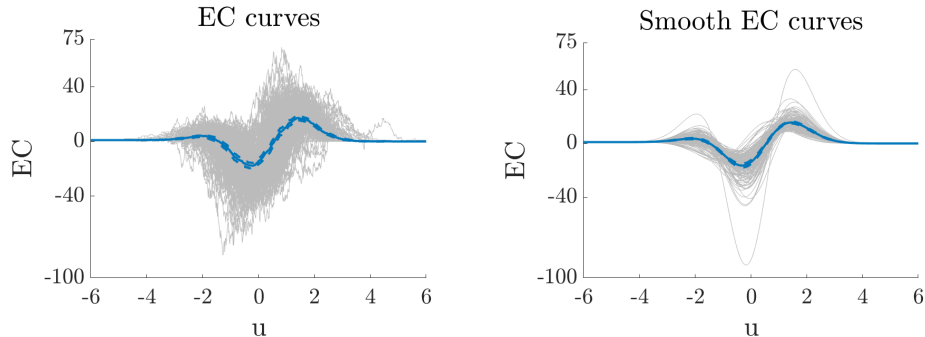


FIG 10. *fMRI example: (Left) Observed EC curves and nonparametric EEC estimate with pointwise confidence bands. (Right) Smooth EC curves and smooth EEC estimate with pointwise confidence bands.*

	$\hat{\mathcal{L}}_1$	$\hat{\mathcal{L}}_2$	$\hat{\mathcal{L}}_3$	u_{FW}	$\chi(z > u_{\text{FW}})$	u_C	$\chi(z > u_C)$
HPE	13.5 ± 1.2	260.1 ± 7.0	642.3 ± 27.0	4.21 ± 0.01	5	3.28 ± 0.01	22
bHPE	12.5	261.3	650.5	4.20	5	3.28	22
SPM12	35.8	315.3	669.0	4.23	5	3.31	20

TABLE 2

Comparison of LKC estimates, corresponding thresholds obtained from the GKF together with EC of excursion sets from the Moran data for HPE, bHPE and SPM12 (IsotE).

estimates of the HPE, which were obtained as the square root of the diagonal entries of $\hat{\Sigma}/N$, as described in Section 2.4. The LKC estimates for bHPE and HPE are fairly close suggesting that deviation from Gaussianity is not strong. However, the estimates from the software package SPM12, which implements IsotE, are substantially different due to non-isotropy and non-stationarity. Interestingly, in this experiment, this does not affect the detection threshold substantially.

Figure 11 shows the activation maps for the thresholds from the bHPE. The FWER map is conservative; the excursion set has EC $\chi(u_{\text{FW}}) = 5$ with no apparent holes, equivalent to 5 connected components, which show as 5 hotspots in the activation map. In comparison, the CER map is less conservative; the excursion set has EC $\chi(u_C) = 22$, again with no apparent holes, equivalent to 22 connected components. The interpretation is that we expect only one connected component to be false.

5.2. *Cosmic Microwave Background Radiation: Isotropic Gaussian field on the sphere.* In cosmology, the EEC plays an important role in summarizing the topological structure of the universe [15, 31, 18, 16, 29, 30]. In

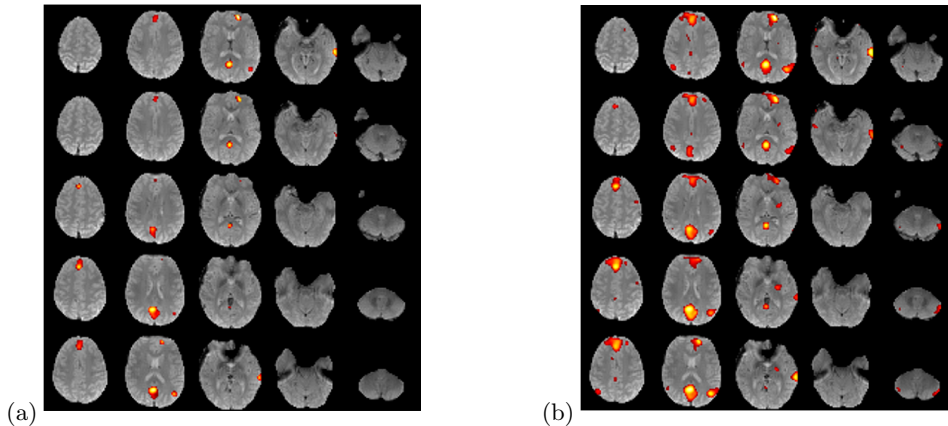


FIG 11. *fMRI activation at a significance level of $FWER=0.05$ (left) and $CER=1$ (right), using the residuals within the brain volume to estimate the EEC. Montage shows the brain volume as transverse slices from the top of the brain (top left panel) to the bottom of the brain (bottom right panel). Colored regions indicate the smoothed Wald statistic field above the threshold. Results are superimposed on an anatomical brain image (gray) for reference.*

particular, the cosmic microwave background (CMB) radiation field gives a glimpse into the early structure of the universe, a short time after the big bang [26]. The goal of this example is to compare the EEC of the observed CMB map to simulated Gaussian fields with the same spatial autocorrelation function, helping assess how close is the observed data to the theoretical model.

For this comparison, we use $N = 1000$ i.i.d. instances of Full Focal Plane 8 (FFP8) simulations, publicly released by the Planck team [28]. These simulations are designed to replicate the observed CMB sky and are based on an isotropic Gaussian random field prescription. To mimic the observation field, in our computer experiments, the CMB maps were contaminated by noise from various sources and then cleaned using the same process as the actual observed data from Planck [27], including smoothing with an isotropic Gaussian kernel with a bandwidth of 180 arcmin. Smoothing makes the distribution of the fields more Gaussian. Additionally, because of contamination by the Milky Way and other large foreground light sources, certain portions of the sky were masked using the most conservative UT78 mask released by the Planck team [26]. For fair comparison, we processed the actual observed CMB field from Planck [27] using the same procedure. Figure 12 shows the observed CMB field rendered over a HEALPix spherical grid with 2048 nodes [14].

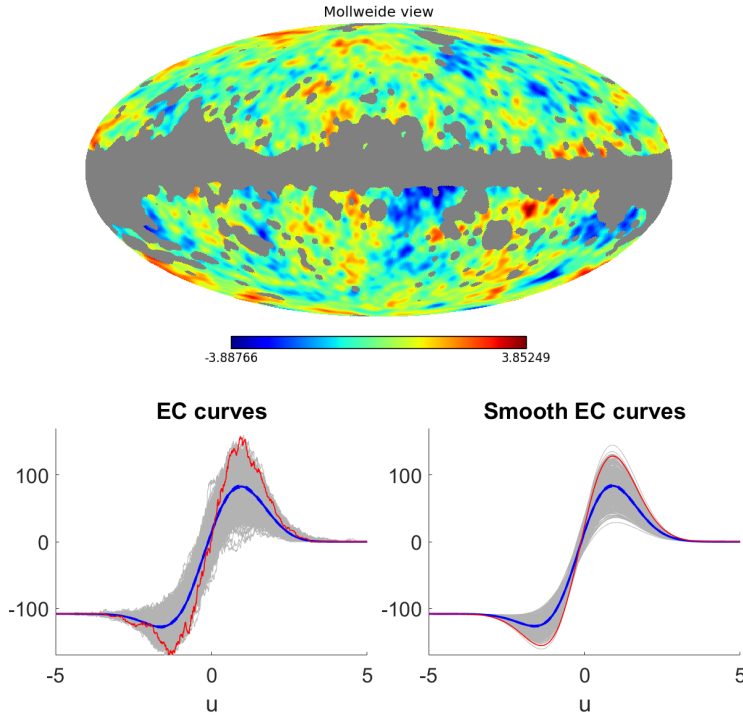


FIG 12. *CMB example: (Top) The observed CMB field on a 2048-resolution HEALPix grid, cleaned and smoothed with a bandwidth of 180 arcmin. (Bottom left) EC curves from $N = 1000$ i.i.d. simulated CMB fields (gray) and nonparametric EEC estimate with pointwise confidence bands (blue). The EC curve corresponding to the Planck data is shown in red. (Bottom right) Smooth EC curves (gray) and smooth EEC estimate (blue) with pointwise confidence bands. The smoothed EC curve from Planck is shown in red.*

The simulated fields and the actual observed field were thresholded at a sequence of thresholds ranging from -5 to 5 in steps of 0.01 and the EC of the resulting excursion sets were computed. Figure 12 shows the observed EC curves and their smoothed versions, together with the nonparametric and parametric estimates of the EEC. The estimated LKCs from the 1000 FFP8 simulations were $\hat{\mathcal{L}}_1 = 426.8 \pm 54.2$ and $\hat{\mathcal{L}}_2 = 1528.9 \pm 346.4$, yielding respective standard errors of 1.7 and 11.0 for the mean LKCs. In contrast, the estimated LKCs from the actual observed field were $\hat{\mathcal{L}}_1^o = 480.3$ and $\hat{\mathcal{L}}_2^o = 2545.0$.

These results have two uses in astronomy. First, the EEC could be used to detect celestial objects against the CMB background [8]. In this case, we obtain $u_{\text{FW}} = 4.279 \pm 0.002$ and $u_{\text{C}} = 3.456 \pm 0.002$. Second, in Figure

12, the observed CMB EC curve (red) is at the edge of the distribution of simulated curves. In fact, the observed $\hat{\mathcal{L}}_2^o$ is 2.93 standard deviations (not standard errors) away from the corresponding estimated mean value $\hat{\mathcal{L}}_2$ from the simulations. This may be evidence that the observed CMB field does not match the physical model that generated the simulations and improvements to the physical model may be necessary [29, 30].

6. Discussion.

6.1. *A linear regression view.* In order to estimate the LKCs, [1] suggested to perform a linear regression of the average field on the EC-densities based on (1). Following that formulation, suppose $\bar{y}(u) = \bar{\chi}^o(u)$ (23) is observed at a discrete set of L levels u_1, \dots, u_L to get the response vector $\bar{\mathbf{y}} = (\bar{y}(u_1), \dots, \bar{y}(u_L))^T$. Similarly, the columns of the design matrix X are the EC densities sampled at the same levels so that $X_{dl} = \rho_d(u_l)$. The linear regression estimator of the vector of LKCs \mathcal{L} is

$$(38) \quad \hat{\mathcal{L}}_{\text{LR}} = (X^T X)^{-1} X^T \bar{\mathbf{y}}.$$

Instead of sampling the EC curves at specific levels, the estimator (13) can be seen as a continuous version of the linear regression estimator in the following way. First, notice that the linear regression estimate $\hat{\mathcal{L}}_{\text{LR}}$, by definition, is the vector $\beta = (\beta_1, \dots, \beta_D)^T$ that minimizes the sum of squares $\sum_{l=1}^L [y_l - \bar{x}_l \beta]^2$, where \bar{x}_l is the l -th row of the matrix X . Respecting the functional form of the EC process, a continuous version of the above sum of squares is the integral $\int_{-\infty}^{\infty} [\bar{y}(u) - \bar{x}(u)\beta]^2 w(u) du$ where $\bar{x}(u) = (\rho_1(u), \dots, \rho_D(u))$ and $w(u)$ is a suitable weight function. Differentiating with respect to β and setting to zero yields that the minimizer is

$$(39) \quad \hat{\beta} = \left[\int_{-\infty}^{\infty} \bar{x}(u)^T \bar{x}(u) w(u) du \right]^{-1} \left[\int_{-\infty}^{\infty} \bar{x}(u)^T \bar{y}(u) w(u) du \right].$$

This solution can be greatly simplified by judiciously choosing $w(u) = e^{u^2/2}$. In this case, the (d, d') entries of the $D \times D$ matrix on the left of (39) are precisely given by (7). This matrix is diagonal and immediately invertible yielding that each of the entries of (39) is the same as the HPE (26).

In other words, the HPE (26) can be seen as a linear regression estimator in the sense of [1] with weight function $e^{u^2/2}$, so that high and low levels u are weighted more heavily than levels u near zero. This may be seen as an advantage in practice because, if the estimated EEC curve is to be used for inference, it is more important to have a better fit at high and low thresholds.

However, as already shown by [1] with other weighting functions, it will be seen in simulations that the weighting function has little practical effect on the estimator.

As far as statistical properties are concerned, note that the ordinary least squares estimator (38) is not necessarily unbiased or consistent, while the HPE (26) always is.

6.2. Advantages over state-of-the-art methods. The main power of the proposed approach is its ability to handle non-stationary fields, like the scale space, and fields defined over non-trivial domains, like the sphere. More complicated domains, like parts of the Earth’s land mass or oceans, or the highly curved cortical surface of the brain, can be handled as long as there is an algorithm to compute the EC of excursion sets over the domain. Being able to handle non-stationary fields can have consequences for analysis choices. In fMRI, for example, assuming non-stationary noise generally makes the results more conservative [12].

A computationally favorable property of the HPE is that, in contrast to the IsotE and WarpE, it does not require numerical derivatives of residual fields nor numerical evaluations of integrals. The only aspect of HPE that is numerically challenging is the computation of EC curves, for which there exist efficient algorithms [17]. In contrast, WarpE requires finding a triangulation of the domain S , which is typically a nontrivial task.

A further advantage of the HPE is that we were able to study theoretical properties as unbiasedness, finite variance, consistency and derive confidence bands for the EEC even in the general non-stationary setting. Moreover, our simulations showed that the bHPE estimator has a similar variance as the WarpE, and in contrast to the latter, seems to be unbiased even in the experimental scenario, which makes the bHPE a better choice for small sample sizes.

6.3. Open theoretical questions.

Conditions for consistency of bHPE. The conditions for consistency of the bHPE seem to be rather abstract and difficult to verify in practice. However, the only unusual condition is **(G5)** for the AGMBF. We conjecture that it might be already implied by conditions **(G1)**-**(G4)** and therefore the bHPE basically requires the same conditions for consistency as are required for the GKF to be valid.

The intuition here is that the residual field R^N has almost surely Morse functions as sample paths. Therefore each field from a sample $R_1^N, \dots, R_N^N \sim R^N$ has a finite number of critical points. Heuristically, this implies that the

number of critical points of the random linear combinations formed from these fields in the AGMBF can be bounded by a finite number depending on the number of critical points of the sample R_1^N, \dots, R_N^N , since situations where these linear combination are not anymore Morse functions with infinitely many critical values do appear with probability zero. Hence this immediately implies finiteness of all moments of the number of critical values.

Unbiasedness of bHPE. In Theorem 2 a) we proved unbiasedness of HPE. This result was one of the main ingredients in Theorem 4 to prove consistency of the bHPE. Our simulations, however, suggest that also the bHPE is unbiased. This requires proving that for fixed $N \in \mathbb{N}$

$$(40) \quad \mathbb{E} \left[\mathcal{L}_d(\hat{\mathcal{G}}) \right] = \mathcal{L}_d(\mathcal{G}),$$

where $\hat{\mathcal{G}}$, respectively \mathcal{G} , is the mean zero, unit variance Gaussian process with covariance function given by the empirical correlation (29) of a sample $f_1, \dots, f_N \sim f$, respectively the correlation of f , and the expectation is with respect to the sample. Since the empirical correlation is unbiased for the true correlation, there is some hope that (40) actually holds true.

Smaller variance of bHPE compared to HPE. As shown in simulation bHPE has almost the same variance as WarpE, because both are computing (through different methods and up to bootstrap sampling) directly the LKCs of the process having the empirical correlation structure of the data as covariance function. Hence the uncertainty in the estimates here is due to the uncertainty in the empirical correlation structure. On the other hand, the uncertainty in the HPE is given by the uncertainty of the EC curves of the samples, which for unknown reasons seems to be higher than the uncertainty in the correlation function.

Variance of the parametric and nonparametric EEC estimators. In simulations we observed that the HPE for the EEC has considerably less variance than its nonparametric counterpart as seen for example in Figure 4. This may be due to the fact that the parametric HPE is, by definition, contained in a finite dimensional space determined by the GKF.

APPENDIX A: PROOFS

A.1. Proof of Theorem 1. Note that $u_0 = \min_{s \in S} f(s)$ and $u_M = \max_{s \in S} f(s)$, then we obtain

$$\begin{aligned}
(41) \quad \frac{(d-1)!}{(2\pi)^{d/2}} \hat{\mathcal{L}}_d &= \int_{-\infty}^{\infty} H_{d-1}(u) (\chi(u) - \mathcal{L}_0 \Phi^+(u)) du \\
&= \int_{u_0}^{u_M} H_{d-1}(u) \chi(u) du - \mathcal{L}_0 \int_{u_0}^{\infty} H_{d-1}(u) \Phi^+(u) du \\
&\quad + \mathcal{L}_0 \int_{-\infty}^{u_0} H_{d-1}(u) (1 - \Phi^+(u)) du.
\end{aligned}$$

Here we used that $\chi(u) = 0$, if $u > u_M$ and $\chi(u) = \mathcal{L}_0$, if $u < u_0$.

Using integration by parts and $H'_d = d \cdot H_{d-1}$ yields for the later two integrals

$$\begin{aligned}
\int_{u_0}^{\infty} H_{d-1}(u) \Phi^+(u) du &= -\Phi^+(u_0) \frac{H_d(u_0)}{d} - \int_{u_0}^{\infty} \frac{H_d(u)}{d} \Phi^{+'}(u) du \\
\int_{-\infty}^{u_0} H_{d-1}(u) (1 - \Phi^+(u)) du &= (1 - \Phi^+(u_0)) \frac{H_d(u_0)}{d} + \int_{-\infty}^{u_0} \frac{H_d(u)}{d} \Phi^{+'}(u) du
\end{aligned}$$

Using the definition of Hermite polynomials $H_d(x) = (-1)^d e^{\frac{x^2}{2}} \frac{d^d}{dx^d} e^{-\frac{x^2}{2}}$ yields

$$\int_{-\infty}^{\infty} \frac{H_d(u)}{d} \frac{e^{-u^2/2}}{\sqrt{2\pi}} du = \frac{(-1)^d}{d\sqrt{2\pi}} \int_{-\infty}^{\infty} \frac{d^d}{dx^d} e^{-\frac{x^2}{2}} du = \frac{(-1)^d}{d\sqrt{2\pi}} \left[\frac{d^{d-1}}{dx^{d-1}} e^{-\frac{u^2}{2}} \right]_{-\infty}^{\infty} = 0.$$

Therefore, equation (41) simplifies to

$$\begin{aligned}
\frac{(d-1)!}{(2\pi)^{d/2}} \hat{\mathcal{L}}_d &= \int_{u_0}^{u_M} H_{d-1}(u) \chi(u) du + \mathcal{L}_0 \frac{H_d(u_0)}{d} - \mathcal{L}_0 \int_{-\infty}^{\infty} \frac{H_d(u)}{d} \frac{e^{-u^2/2}}{\sqrt{2\pi}} du \\
&= \int_{u_0}^{u_M} H_{d-1}(u) \chi(u) du + \mathcal{L}_0 \frac{H_d(u_0)}{d}
\end{aligned}$$

and thus using the representation (12) we finally compute:

$$\begin{aligned}
\frac{d!}{(2\pi)^{d/2}} \hat{\mathcal{L}}_d &= \mathcal{L}_0 H_d(u_0) + \sum_{m=1}^M a_m (H_d(u_m) - H_d(u_{m-1})) \\
&= \mathcal{L}_0 H_d(u_0) + \sum_{m=1}^M a_m H_d(u_m) - \sum_{m=0}^{M-1} a_{m+1} H_d(u_m) \\
&= \sum_{m=0}^M (a_m - a_{m+1}) H_d(u_m),
\end{aligned}$$

where we defined $a_0 = \mathcal{L}_0$ and $a_{M+1} = 0$. □

A.2. Proof of Theorem 2. Part 1):

By equation (4) we have to justify interchanging the integral and the expectation in

$$\begin{aligned} \frac{(d-1)!}{(2\pi)^{d/2}} \mathbb{E} [\hat{\mathcal{L}}_d] &= \mathbb{E} \left[\int_{-\infty}^{\infty} H_{d-1}(u) (\chi(u) - \mathcal{L}_0 \Phi^+(u)) du \right] \\ &= \int_{-\infty}^{\infty} H_{d-1}(u) (\text{EEC}(u) - \mathcal{L}_0 \Phi^+(u)) du = \frac{(d-1)!}{(2\pi)^{d/2}} \mathcal{L}_d. \end{aligned}$$

Therefore, we consider the following splitting of the integral

$$\begin{aligned} \frac{(d-1)!}{(2\pi)^{d/2}} \hat{\mathcal{L}}_d &= \int_{u_0}^{u_M} H_{d-1}(u) \chi(u) du - \mathcal{L}_0 \int_{u_0}^{\infty} H_{d-1}(u) \Phi^+(u) du \\ &\quad + \mathcal{L}_0 \int_{-\infty}^{u_0} H_{d-1}(u) (1 - \Phi^+(u)) du \\ &= I + \mathcal{L}_0 \cdot II + \mathcal{L}_0 \cdot III, \end{aligned}$$

where as above $u_0 = \min_{s \in S} f(s)$. For each summand we show separately that we can interchange the expectation and the integral, if we write it using characteristic functions.

We begin with integral I. Here it is sufficient to prove that

$$(42) \quad \int_{-\infty}^{\infty} \mathbb{E} [\mathbf{1}_{(u_0, u_M]}(u) |H_{d-1}(u) \chi(u)|] du < \infty.$$

Again we use the stepfunction representation (12) and note that $|a_m| \leq M_0 = M + \mathcal{L}_0$ for all $m = 1, \dots, M$. Thus, using (G5a), the triangle inequality,

Hölder's inequality and Borel-TIS inequality, we obtain for any $\epsilon > 0$

$$\begin{aligned}
& \int_{-\infty}^{\infty} \mathbb{E} \left[\mathbb{1}_{(u_0, u_M]}(u) |H_{d-1}(u)\chi(u)| \right] du \\
& \leq \int_{-\infty}^{\infty} \mathbb{E} \left[\sum_{m=1}^M |a_m| \mathbb{1}_{(u_{m-1}, u_m]}(u) \right] |H_{d-1}(u)| du \\
& < \int_{-\infty}^{\infty} \mathbb{E} [M_0 \mathbb{1}_{(u_0, u_M]}(u)] |H_{d-1}(u)| du \\
& \leq \int_{-\infty}^{\infty} \mathbb{E} [M_0^{1+\epsilon}]^{\frac{1}{1+\epsilon}} \mathbb{E} [\mathbb{1}_{(u_0, u_M]}(u)]^{\frac{1}{1+1/\epsilon}} |H_{d-1}(u)| du \\
& \leq C' \int_{-\infty}^{\infty} P \left[\min_{s \in S} f(s) < u \leq \max_{s \in S} f(s) \right]^{\frac{1}{1+1/\epsilon}} |H_{d-1}(u)| du \\
& \leq C' \int_{-\infty}^{\mathbb{E}[u_0]} e^{\frac{-(u-\mathbb{E}[u_0])^2}{2+2/\epsilon}} |H_{d-1}(u)| du + C' \int_{\mathbb{E}[u_0]}^{\mathbb{E}[u_M]} |H_{d-1}(u)| du + \\
& \quad C' \int_{\mathbb{E}[u_M]}^{\infty} e^{\frac{-(u-\mathbb{E}[u_M])^2}{2+2/\epsilon}} |H_{d-1}(u)| du < \infty.
\end{aligned}$$

Thus, for I we are allowed to interchange integral and expectation. Note that we used

$$\begin{aligned}
P \left[\min_{s \in S} f(s) < u \right] & \leq e^{-\frac{(-u+\mathbb{E}[u_0])^2}{2\sigma_T^2}}, \quad \text{for } u < \mathbb{E} \left[\min_{s \in S} f(s) \right] \\
P \left[\max_{s \in S} f(s) > u \right] & \leq e^{-\frac{(u-\mathbb{E}[u_M])^2}{2}}, \quad \text{for } u > \mathbb{E} \left[\max_{s \in S} f(s) \right],
\end{aligned}$$

which are easily derived from Borel-TIS inequality (e.g., Adler and Taylor [2, Thm. 2.1.1]). Note that $\sigma_T^2 = 1$ in our case.

Next consider II and III. Note that similarly as above using Borel-TIS and the exponential bounds for $\Phi^+(u)$ and $1 - \Phi^+(u)$, we compute

$$\begin{aligned}
& \int_{-\infty}^{\infty} \mathbb{E} \left[\mathbb{1}_{(u_0, \infty)}(u) |H_{d-1}(u)| \Phi^+(u) \right] du \\
& \leq \int_{-\infty}^{\infty} |H_{d-1}(u)| \Phi^+(u) P \left[\min_{s \in S} f(s) < u \right] du \\
& \leq \int_{-\infty}^{\mathbb{E}[u_0]} e^{\frac{-(u-\mathbb{E}[u_0])^2}{2}} |H_{d-1}(u)| du + \int_{\mathbb{E}[u_0]}^{\infty} |H_{d-1}(u)| \Phi^+(u) du < \infty.
\end{aligned}$$

and

$$\begin{aligned}
& \int_{-\infty}^{\infty} \mathbb{E} \left[\mathbf{1}_{(-\infty, u_0)}(u) |H_{d-1}(u)| (1 - \Phi^+(u)) \right] du \\
& \leq \int_{-\infty}^{\infty} |H_{d-1}(u)| (1 - \Phi^+(u)) P \left[\min_{s \in S} f(s) > u \right] du \\
& \leq \int_{-\infty}^{\mathbb{E}[u_M]} (1 - \Phi^+(u)) |H_{d-1}(u)| du \\
& \quad + \int_{\mathbb{E}[u_M]}^{\infty} |H_{d-1}(u)| P \left[\max_{s \in S} f(s) > u \right] du < \infty.
\end{aligned}$$

Part 2):

Note that by part 1) we have

$$\sigma_{dd'} = \text{Cov} \left[\hat{\mathcal{L}}_d, \hat{\mathcal{L}}_{d'} \right] = \mathbb{E} \left[\hat{\mathcal{L}}_d \hat{\mathcal{L}}_{d'} \right] - \mathcal{L}_d \mathcal{L}_{d'}.$$

Hence we will only show that the expectation on the r.h.s. is finite. With slight but obvious change in notation to part 1) we can write

$$\frac{(d-1)!^2}{(2\pi)^d} \mathbb{E} \left[\hat{\mathcal{L}}_d \hat{\mathcal{L}}_{d'} \right] = \mathbb{E} \left[(I_d + \mathcal{L}_0 \cdot II_d + \mathcal{L}_0 \cdot III_d)(I_{d'} + \mathcal{L}_0 \cdot II_{d'} + \mathcal{L}_0 \cdot III_{d'}) \right]$$

Our strategy is again to bound each summand separately and even more show that we could interchange expectation and integration, since this implies immediately the finiteness. The arguments are very similar to the unbiasedness proof. Therefore we shorten the computations considerably. Moreover, we use the abbreviation $P(u, u') = |H_{d-1}(u)H_{d'-1}(u')|$.

Case $\mathbb{E}[I_d I_{d'}]$:

$$\begin{aligned}
& \iint_{\mathbb{R}^2} P(u, u') \mathbb{E} \left[\mathbf{1}_{(u_0, u_M]}(u) \mathbf{1}_{(u_0, u_M]}(u') |\chi(u)\chi(u')| \right] dud u' \\
& < \iint_{\mathbb{R}^2} P(u, u') \mathbb{E} \left[M_0^2 \mathbf{1}_{(u_0, u_M]}(u) \mathbf{1}_{(u_0, u_M]}(u') \right] dud u' \\
& \leq \iint_{\mathbb{R}^2} P(u, u') \mathbb{E} \left[M_0^{2+\epsilon} \right]^{\frac{2}{2+\epsilon}} \mathbb{E} \left[\mathbf{1}_{(u_0, u_M]}(u) \mathbf{1}_{(u_0, u_M]}(u') \right]^{\frac{1}{1+2/\epsilon}} dud u' \\
& \leq \iint_{\mathbb{R}^2} P(u, u') \mathbb{E} \left[M_0^{2+\epsilon} \right]^{\frac{2}{2+\epsilon}} \mathbb{E} \left[\mathbf{1}_{(u_0, u_M]}(u) \right]^{\frac{1}{2+4/\epsilon}} \mathbb{E} \left[\mathbf{1}_{(u_0, u_M]}(u') \right]^{\frac{1}{2+4/\epsilon}} dud u' \\
& \leq C \int_{-\infty}^{\infty} |H_{d-1}(u)| P \left[\min_{s \in S} f(s) < u \leq \max_{s \in S} f(s) \right]^{\frac{1}{2+4/\epsilon}} du \\
& \quad \cdot \int_{-\infty}^{\infty} |H_{d'-1}(u')| P \left[\min_{s \in S} f(s) < u' \leq \max_{s \in S} f(s) \right]^{\frac{1}{2+4/\epsilon}} du' < \infty
\end{aligned}$$

Case E $[II_d III_{d'}]$:

$$\begin{aligned}
& \iint_{\mathbb{R}^2} P(u, u') \Phi^+(u) \Phi^+(u') \mathbb{E} [\mathbb{1}_{(u_0, \infty)}(u) \mathbb{1}_{(u_0, \infty)}(u')] \, dud u' \\
& \leq \iint_{\mathbb{R}^2} P(u, u') \Phi^+(u) \Phi^+(u') P \left[\min_{s \in S} f(s) < u \right]^{\frac{1}{2}} P \left[\min_{s \in S} f(s) < u' \right]^{\frac{1}{2}} \, dud u' \\
& \leq \int_{\mathbb{R}} |H_{d-1}(u)| \Phi^+(u) P \left[\min_{s \in S} f(s) < u \right]^{\frac{1}{2}} \, du \cdot \int_{\mathbb{R}} |H_{k-1}(u')| \Phi^+(u') P \left[\min_{s \in S} f(s) < u' \right]^{\frac{1}{2}} \, du' \\
& < \infty.
\end{aligned}$$

Case E $[III_d III_{d'}]$: Reduces again basically, by the same arguments as in the previous case to the integrals III.

Case E $[I_d III_{d'}]$:

$$\begin{aligned}
& \iint_{\mathbb{R}^2} P(u, u') \Phi^+(u') \mathbb{E} [\mathbb{1}_{(u_0, u_M)}(u) \mathbb{1}_{[u_0, \infty)}(u') |\chi(u)|] \, dud u' \\
& \leq \iint_{\mathbb{R}^2} P(u, u') \Phi^+(u') \mathbb{E} [M_0^{2+\epsilon}]^{\frac{2}{2+\epsilon}} \mathbb{E} [\mathbb{1}_{(u_0, u_M)}(u)]^{\frac{1}{2+4/\epsilon}} \mathbb{E} [\mathbb{1}_{[u_0, \infty)}(u')]^{\frac{1}{2+4/\epsilon}} \, dud u' \\
& \leq C \int_{-\infty}^{\infty} |H_{d-1}(u)| P \left[\min_{s \in S} f(s) < u \leq \max_{s \in S} f(s) \right]^{\frac{1}{2+4/\epsilon}} \, du \\
& \quad \cdot \int_{\mathbb{R}} |H_{k-1}(u')| \Phi^+(u') P \left[\min_{s \in S} f(s) < u' \right]^{\frac{1}{2+4/\epsilon}} \, du' < \infty
\end{aligned}$$

Case E $[(I_d III_{d'})]$ and E $[(II_d III_{d'})]$: basically, the same arguments as previous one.

Thus, by Fubini we have $\sigma_{dd'} < \infty$. \square

A.3. Proof of Corollary 1. The computations in the proof of Theorem 2 2.) are valid for all $d, k \in \mathbb{N}$ and imply that the identity (11) is true, i.e. interchanging the integrals is justified. This, implies

$$\frac{(2\pi)^{d/2} (2\pi)^{d'/2}}{(d-1)!(k-1)!} \iint H_{d-1}(u) H_{k-1}(v) \text{Cov} [\chi(u), \chi(v)] \, du \, dv < \infty$$

for all $d, k \in \mathbb{N}$. However, this can only be true, if $\text{Cov} [\chi(u), \chi(v)]$ decays faster for $u, u' \rightarrow \pm\infty$ than any polynomial in u, u' . \square

A.4. Proof of Theorem 3.

- (i) It follows from the expressions of $\text{EEC}(u)$ and $\widehat{\text{EEC}}^{(N)}(u)$ in equations (1) and (18) that, for any $\varepsilon > 0$,

$$\begin{aligned}
 & \mathbb{P} \left[\sup_u |\widehat{\text{EEC}}^{(N)}(u) - \text{EEC}(u)| > \varepsilon \right] \\
 (43) \quad & \leq \mathbb{P} \left[\sum_{j=1}^N \sup_u |\hat{\mathcal{L}}_d \rho_d(u) - \mathcal{L}_d \rho_d(u)| > \varepsilon \right] \\
 & \leq \sum_{j=1}^N \mathbb{P} \left[\sup_u |\rho_d(u)| |\hat{\mathcal{L}}_d - \mathcal{L}_d| > \varepsilon/N \right],
 \end{aligned}$$

where we have used the triangle inequality and the fact if the sum of N terms is greater than ε , then at least one of the terms should be greater than ε/N . Notice that for $j = 1, \dots, N$, $\rho_d(u)$ is bounded in $u \in R$ and $\hat{\mathcal{L}}_d$ converges to \mathcal{L}_d in probability. Therefore, (43) tends to 0, yielding that $\widehat{\text{EEC}}^{(N)}(u)$ is a uniformly consistent estimator of $\text{EEC}(u)$. The uniform consistency of $\widehat{\text{EEC}}^{(N)}(u)$ follows similarly.

- (ii) Replacing (18), let

$$G^{(N)}(u) = \sqrt{N} \left[\widehat{\text{EEC}}^{(N)}(u) - \text{EEC}(u) \right] = \sum_{j=1}^N Z_j^{(N)} \rho_d(u),$$

where

$$(44) \quad Z_j^{(N)} = \sqrt{N} \left(\hat{\mathcal{L}}_j^{(N)} - \mathcal{L}_d \right).$$

By the multivariate CLT (14), for any positive integer k and real numbers u_1, \dots, u_k ,

$$(G^{(N)}(u_1), G^{(N)}(u_2), \dots, G^{(N)}(u_k)) \xrightarrow{D} (G(u_1), G(u_2), \dots, G(u_k)),$$

where $G(u)$ is given in (21). This gives convergence in finite dimensional distribution. To prove convergence as a stochastic process, we apply a version of Prokhorov's Theorem [5, Thm 4.10] on the space of continuous functions. Since the $\rho_d(u)$ are uniformly Lipschitz continuous in u , the following compactness inequality holds for all $h > 0$ and

N ,

$$\begin{aligned} & \sup_{-\infty < u < u+h < \infty} \mathbb{E} \left[G^{(N)}(u+h) - G^{(N)}(u) \right]^2 \\ &= \sup_{-\infty < u < u+h < \infty} \mathbb{E} \left\{ \sum_{j=1}^N Z_j^{(N)} [\rho_d(u+h) - \rho_d(u)] \right\}^2 \\ &\leq \left(N^2 \max_{1 \leq j \leq N} \sigma_{jj} \right) K_0 h^2 \leq K h^2, \end{aligned}$$

where K_0, K are positive constants and we have used Cauchy-Schwarz inequality. Note that the variances $\sigma_{jj}, j = 1, \dots, N$ are finite. This gives the tightness condition and the result follows. \square

\square

A.5. Proof of Theorem 4. 1.) This is a simple computation.

2.) We can for almost all sets of residuals R_1^N, \dots, R_N^N apply Theorem 2a) to the AGMBF, which yields that almost surely $\mathbb{E} \left[\hat{\mathcal{L}}(R_N^{*,g_m}) \right] = \mathcal{L}(R_N^{*,g_m}) < \infty$ and therefore the SLLN implies the claim.

3.) Note that the LKCs as defined in [2, eq. 12.4.7] and as they appear in the GKF are integrals of continuous functions over S . The volume elements \mathcal{H}_j do depend only on the Riemannian metric induced by the random field, which is in local coordinates $\partial_1, \dots, \partial_D$ given by

$$\hat{g}_{dd'}(s) = \mathbb{E} \left[\partial_d R_N^{*,g_m}(s) \partial_{d'} R_N^{*,g_m}(s) \right] = \partial_d \partial_{d'} \hat{\mathbf{r}}(s, s')|_{s=s'}$$

The latter does converge by **(R5)** almost surely uniformly to

$$\partial_d \partial_{d'} \mathbf{r}(s, s')|_{s=s'} = \mathbb{E} \left[\partial_d G(s) \partial_{d'} G(s) \right] = g_{dd'}(s).$$

The only other random quantity in the integral is the Riemannian curvature tensor, which by [2, p.308, first equation] is a continuous function depending on

$$\begin{aligned} \mathbb{E} \left[\partial_d \partial_{d'} R_N^{*,g_m}(s) \partial_{d''} \partial_{d'''} R_N^{*,g_m}(s) \right] &= \partial_d^s \partial_{d'}^s \partial_{d''}^{s'} \partial_{d'''}^{s'} \hat{\mathbf{r}}(s, s')|_{s=s'} \\ &\xrightarrow{a.s.} \partial_d^s \partial_{d'}^s \partial_{d''}^{s'} \partial_{d'''}^{s'} \mathbf{r}(s, s')|_{s=s'} \end{aligned}$$

for all $d, d', d'', d''' \in \{1, \dots, D\}$, where the superscript in ∂_d^s indicates to which of the two components the partial derivative is applied to.

Since all the above convergences are uniformly almost surely, we can apply Lebesgue's dominated convergence theorem in order to interchange the limit N tending to infinity and the integrals in order to obtain the claim $\mathcal{L}(R_N^{*,g}) \xrightarrow{a.s.} \mathcal{L}(\mathcal{G}(0, \mathbf{r}))$. \square

A.6. Proof of Theorem 5.

PROOF. The result follows from applying Lemma 1 below with $\hat{g}(u) = \widehat{\text{EEC}}^{(N)}(u) - \alpha$ and $g(u) = \text{EEC}(u) - \alpha$. The conditions of the lemma are satisfied by these functions by Theorem 3. \square

LEMMA 1. *Let the function $\hat{g}^{(N)}(u)$ and its first derivative $\hat{g}'^{(N)}(u)$ be uniformly consistent estimators of the function $g(u)$ and its first derivative $g'(u)$, respectively, where both are uniformly continuous over $u \in \mathbb{R}$. Assume there exists an open interval $I = (a, b)$ such that g is strictly monotone on I and there exists a unique solution $u_0 \in I$ to the equation $g(u) = 0$. Define $\hat{u}^{(N)} = \sup\{u \in I : \hat{g}^{(N)}(u) = 0\}$.*

- (i) \hat{u} is a consistent estimator of u_0 .
- (ii) Suppose the derivative $g'(u_0) \neq 0$. If $\sqrt{N}[\hat{g}^{(N)}(u) - g(u)]$ converges uniformly in distribution to a Gaussian process $G(u)$, then $\sqrt{N}(\hat{u}^{(N)} - u_0)$ converges in distribution to $G(u_0)/g'(u_0)$.

PROOF.

- (i) Without loss of generality, assume that g is strictly decreasing on I . For any $\varepsilon > 0$, $g(u_0 - \varepsilon) > 0 > g(u_0 + \varepsilon)$ since $g(u_0) = 0$. Since $\hat{g}^{(N)}(u)$ is a consistent estimator of $g(u)$, we have

$$\mathbb{P} \left[\hat{g}^{(N)}(u_0 - \varepsilon) > 0 > \hat{g}^{(N)}(u_0 + \varepsilon) \right] \rightarrow 1,$$

implying that with probability tending to 1, there is a root of \hat{g} in $I_{0,\varepsilon} = (u_0 - \varepsilon, u_0 + \varepsilon)$. On the other hand, by the monotonicity of g , there exists $\delta > 0$ such that

$$\inf_{u \in I \setminus I_{0,\varepsilon}} |g(u)| > \delta.$$

Further, by the uniform consistency of \hat{g} ,

$$\mathbb{P} \left[\sup_{u \in I} |\hat{g}^{(N)}(u) - g(u)| < \delta/2 \right] \rightarrow 1.$$

Therefore, since

$$\inf_{u \in I \setminus I_{0,\varepsilon}} |\hat{g}^{(N)}(u)| \geq \inf_{u \in I \setminus I_{0,\varepsilon}} |g(u)| - \sup_{u \in I \setminus I_{0,\varepsilon}} |\hat{g}^{(N)}(u) - g(u)|,$$

we have that

$$\begin{aligned} & \mathbb{P} \left[\inf_{u \in I \setminus I_{0,\varepsilon}} |\hat{g}^{(N)}(u)| > \delta/2 \right] \\ & \geq \mathbb{P} \left[\inf_{u \in I \setminus I_{0,\varepsilon}} |g(u)| - \sup_{u \in I \setminus I_{0,\varepsilon}} |\hat{g}^{(N)}(u) - g(u)| > \delta/2 \right] \\ & = \mathbb{P} \left[\sup_{u \in I \setminus I_{0,\varepsilon}} |\hat{g}^{(N)}(u) - g(u)| < \inf_{u \in I \setminus I_{0,\varepsilon}} |g(u)| - \delta/2 \right] \rightarrow 1. \end{aligned}$$

This implies that with probability tending to 1, there is no root of $\hat{g}^{(N)}$ outside $I_{0,\varepsilon}$. From the definition of $\hat{u}^{(N)}$, we obtain that $\hat{u}^{(N)}$ is the only root of $\hat{g}^{(N)}$ in I with probability tending to 1. Thus

$$\mathbb{P}[|\hat{u}^{(N)} - u_0| < \varepsilon] = \mathbb{P}[\hat{u}^{(N)} \in I_{0,\varepsilon}] \rightarrow 1,$$

yielding that \hat{u} is a consistent estimator of u_0 .

(ii) By a Taylor expansion of $\hat{g}^{(N)}(u)$ around u_0 ,

$$0 = \hat{g}^{(N)}(\hat{u}) = \hat{g}^{(N)}(u_0) + (\hat{u}^{(N)} - u_0)\hat{g}'^{(N)}(u^*),$$

where u^* is between u_0 and \hat{u} , i.e. $|u^* - u_0| \leq |\hat{u}^{(N)} - u_0|$. Rearranging, and since $g(u_0) = 0$,

$$(45) \quad \sqrt{N}(\hat{u}^{(N)} - u_0) = -\frac{\sqrt{N}[\hat{g}^{(N)}(u_0) - g(u_0)]}{\hat{g}'^{(N)}(u^*)}.$$

The numerator converges to $G(u)$ in distribution by assumption. To see that the denominator converges to $g'(u_0)$ in probability,

$$(46) \quad \begin{aligned} \hat{g}'^{(N)}(u^*) &= g'(u_0) + [\hat{g}'^{(N)}(u^*) - g'(u_0)] \\ &= g'(u_0) + [\hat{g}'^{(N)}(u^*) - g'(u^*)] + [g'(u^*) - g'(u_0)] \rightarrow g'(u_0), \end{aligned}$$

since $\hat{g}'^{(N)}(u^*) - g'(u^*)$ and $g'(u^*) - g'(u_0)$ converge to 0 in probability by the uniform consistency of $\hat{g}^{(N)}$ and by part (i) of the lemma, respectively. The result follows immediately from (45) and (46). \square

ACKNOWLEDGMENTS

A.S., D.C. and F.T. were partially supported by NIH grant R01EB026859.

REFERENCES

- [1] Robert J. Adler, Kevin Bartz, Sam C. Kou and Anthea Monod. Estimating Thresholding Levels for Random Fields via Euler Characteristics. <https://arxiv.org/abs/1704.08562>, 2015.
- [2] Robert J. Adler and Jonathan E. Taylor, Random Fields and Geometry, Springer, 2007.
- [3] Robert J. Adler, Jonathan E. Taylor, and Keith J. Worsley. Applications of random fields and geometry: Foundations and case studies. 2010.
- [4] Jean-Marc Azaïs and Céline Delmas, Asymptotic expansions for the distribution of the maximum of Gaussian random fields. *Extremes* **5**, p.181–212, 2002.
- [5] Jean-Marc Azaïs and Mario Wschebor Level sets and extrema of random processes and fields, John Wiley & Sons, Inc., 2009.
- [6] Edward T. Bullmore, John Suckling, Stephan Overmeyer, Sophia Rabe-Hesketh, Eric Taylor, Michael J. Brammer. Global, voxel, and cluster tests, by theory and permutation, for a difference between two groups of structural MR images of the brain. *IEEE Transactions on Medical Imaging* **18**, p.32–42, 1999.
- [7] Dan Cheng and Armin Schwartzman. Multiple Testing of Local Maxima for Detection of Peaks in Random Fields. *The Annals of Statistics* **45**(2), p.529–556, 2017.
- [8] Dan Cheng, Valentina Cammarota, Yabebal Fantaye, Domenico Marinucci, and Armin Schwartzman. Multiple Testing of Local Maxima for Detection of Peaks on the (Celestial) Sphere. *Bernoulli* **45**(2), p.529–556, 2017.
- [9] Dan Cheng and Yimin Xiao, The mean Euler characteristic and excursion probability of Gaussian random fields with stationary increments. *The Annals of Applied Probability* **26**, p.722–759, 2016.
- [10] David A. Degras, Simultaneous confidence bands for nonparametric regression with functional data. *Statistica Sinica*, p.1735-1765, 2011.
- [11] Friedhelm Eicker. Asymptotic Normality and Consistency of the Least Squares Estimators for Families of Linear Regressions. *The Annals of Mathematical Statistics* **34**(2), 447–456, 1963.
- [12] Anders Eklund, Thomas E. Nichols, and Hans Knutsson. Cluster failure: Why fMRI inferences for spatial extent have inflated false-positive rates. *PNAS*, **113** (28), p.7900–7905, 2016.
- [13] Anne Estrade and Julie Fournier. Number of critical points of a Gaussian random field: Condition for a finite variance. *Statistics & Probability Letters*. **118**, p.94–99, 2016.
- [14] Krzysztof M. Gorski, Eric Hivon, Anthony J. Banday, Benjamin D. Wandelt, Frode K. Hansen, Mstvos Reinecke, and Matthia Bartelmann. HEALPix: A Framework for High-Resolution Discretization and Fast Analysis of Data Distributed on the Sphere. *The Astrophysical Journal*, **622**(2), p.759–771, 2005.
- [15] J. Richard Gott, Adrian L. Melott, and Mark Dickinson. The sponge-like topology of large-scale structure in the universe. *The Astrophysical Journal*, **306**, p.341–357, 1986.
- [16] J. Richard Gott, Yun-Young Choi, Changbom Park, and Juhan Kim. Three-dimensional genus topology of luminous red galaxies. *The Astrophysical Journal Letters*, **695**(1), p.L45–L48, 2009.
- [17] T. Heiss, H. Wagner. Streaming Algorithm for Euler Characteristic Curves of Multi-dimensional Images. *International Conference on Computer Analysis of Images and Patterns*, p.397–409, Springer, Cham, 2017.
- [18] Chiaki Hikage, Yasushi Suto, Issha Kayo, Atsushi Taruya, Takahiko Matsubara,

- Michael S. Vogeley, Fiona Hoyle, J. Richard Gott, Jon Brinkmann, and SDSS collaboration. Three-dimensional genus statistics of galaxies in the sdss early data release. *Publications of the Astronomical Society of Japan*, **54**(5) p.707–717, 2002.
- [19] Stefan J. Kiebel, Jean-Baptiste Poline, Karl J. Friston, Andrew P. Holmes, and Keith J. Worsley. Robust smoothness estimation in statistical parametric maps using standardized residuals from the general linear model. *Neuroimage* **10**(6), p.756–766, 1999.
- [20] Gregory Leibon, Daniel N. Rockmore, Wooram Park, Robert Taintor, Gregory S. Chirikjian. A fast Hermite transform. *Theoretical Computer Science* **409**, p.211–228, 2008.
- [21] Jean-Bernard Martens. The Hermite Transform: A Survey. *EURASIP Journal on Applied Signal Processing*, Volume 2006, p. 1–20.
- [22] Joseph M. Moran, Eshin Jolly, and Jason P. Mitchell. Social-cognitive deficits in normal aging. *Journal of Neuroscience*, **32**(16), p.5553–5561, 2012.
- [23] Thomas E. Nichols. Multiple testing corrections, nonparametric methods, and random field theory. *Neuroimage*, **62**(2), p. 811–815, 2012.
- [24] V. I. Piterbarg. Rice’s method for large excursions of Gaussian random fields. Technical Report NO. 478, Center for Stochastic Processes, Univ. North Carolina, 1996.
- [25] David Pollard. Empirical processes: theory and applications, NSF-CBMS regional conference series in probability and statistics. Institute of Mathematical Statistics and the American Statistical Association, 1990.
- [26] Peter AR Ade, Nabila Aghanim, C. Armitage-Caplan, Monique Arnaud, M. Ashdown, F. Atrio-Barandela, J. Aumont et al.. Planck 2013 results. XXIII. Isotropy and statistics of the CMB. *Astronomy & Astrophysics* **571**(A23), 2014.
- [27] Planck Collaboration, R. Adam, P. A. R. Ade, N. Aghanim, M. Arnaud, M. Ashdown, J. Aumont, C. Baccigalupi, A. J. Banday, R. B. Barreiro, and et al. Planck 2015 results. IX. Diffuse component separation: CMB maps. *Astronomy & Astrophysics*, **594**(A9), 2016.
- [28] Planck Collaboration, P. A. R. Ade, N. Aghanim, M. Arnaud, M. Ashdown, J. Aumont, C. Baccigalupi, A. J. Banday, R. B. Barreiro, J. G. Bartlett, and et al. Planck 2015 results. XII. Full focal plane simulations. *Astronomy & Astrophysics*, **594**(A12), 2016.
- [29] Pratyush Pranav, Herbert Edelsbrunner, Rien Van de Weygaert, Gert Vegter, Michael Kerber, Bernard JT Jones, and Mathijs Wintraecken. The topology of the cosmic web in terms of persistent Bettinnumbers. *Monthly Notices of the Royal Astronomical Society*, **465**(4) 4281–4310, 2016.
- [30] Pratyush Pranav, Robert J. Adler, Thomas Buchert, Herbert Edelsbrunner, Bernard JT Jones, Armin Schwartzman, Hubert Wagner, and Rien Van de Weygaert. Unexpected topology of the temperature fluctuations in the cosmic microwave background. *Astronomy & Astrophysics*, **627**, p.A163, 2019.
- [31] James E. Rhoads, J. Richard Gott III, and Marc Postman. The genus curve of the abell clusters. *The Astrophysical Journal*, **421** p.1–8, 1994.
- [32] David O. Siegmund and Keith J. Worsley. Testing for a Signal with Unknown Location and Scale in a Stationary Gaussian Random Field. *The Annals of Statistics*, **23**(2), 608-639, 1995.
- [33] Max Sommerfeld, Stephen Sain and Armin Schwartzman. Confidence regions for spatial excursion sets from repeated random field observations, with an application to climate. *Journal of the American Statistical Association*, **113**(523), 1327-1340.
- [34] Michel Ledoux and Michel Talagrand. Probability in Banach Spaces: isoperimetry and processes, Springer Science & Business Media, 2013
- [35] Jonathan E. Taylor, Akimichi Takemura, and Robert J. Adler. Validity of the ex-

- pected Euler characteristic heuristic. *The Annals of Probability*, **33**(4), 1362–1396, 2005.
- [36] Jonathan E. Taylor and Keith J. Worsley. Detecting Sparse Signals in Random Fields, With an Application to Brain Mapping. *Journal of the American Statistical Association*, **102**(479), p.913–928, 2007.
- [37] Fabian J.E. Telschow and Armin Schwartzman. Simultaneous Confidence Bands for Functional Data Using the Gaussian Kinematic Formula. *arXiv preprint arXiv:1901.06386* (2019).
- [38] Van der Vaart, A. W., Asymptotic statistics, Cambridge university press, 2000.
- [39] Keith J. Worsley, Sean Marrett, Peter Neelin, Alain C. Vandal, Karl J. Friston, and Alan C. Evans. A unified statistical approach for determining significant signals in images of cerebral activation. *Human Brain Mapping*, **4**(1), p.58–73, 1996.
- [40] Keith J. Worsley. An Unbiased Estimator for the Roughness of a Multivariate Gaussian Random Field. *Technical report, Department of Mathematics and Statistics, McGill University*.
- [41] Keith J. Worsley, Sean Marrett, Peter Neelin, Alain C. Vandal, Karl J. Friston, and Alan C. Evans. Detecting changes in nonisotropic images. *Human Brain Mapping*, **8**(2-3) p.98–101, 1999.
- [42] Keith J. Worsley, Jonathan E. Taylor, Francesco Tomaiuolo, and Jason Lerch. Unified univariate and multivariate random field theory. *Neuroimage*, **23** S189–195, 2004.

DIVISION OF BIostatISTICS AND HALICIOĞLU DATA SCIENCE INSTITUTE UNIVERSITY OF CALIFORNIA, SAN DIEGO 9500 GILMAN DRIVE LA JOLLA, CA 92093 USA E-MAIL: armins@ucsd.edu E-MAIL: ftelschow@ucsd.edu	SCHOOL OF MATHEMATICAL AND STATISTICAL SCIENCES ARIZONA STATE UNIVERSITY TEMPE, AZ 85287-1804 USA E-MAIL: cheng.stats@gmail.com
---	--

DÉPARTEMENT DE PHYSIQUE
ECOLE NORMALE SUPÉRIEURE DE LYON
15 PARVIS RENÉ DESCARTES
69342 LYON
FRANCE
E-MAIL: pratyush.pranav@ens-lyon.fr